Energy & Environmental Science

ROYAL SOCIETY OF CHEMISTRY

PAPER

View Article Online
View Journal | View Issue

Cite this: *Energy Environ. Sci.*, 2024, **17**, 9215

From generation to collection – impact of deposition temperature on charge carrier dynamics of high-performance vacuum-processed organic solar cells†

Richard Adam Pacalaj, *[a] Yifan Dong, ‡[a] Ivan Ramirez,[b] Roderick C. I. MacKenzie,[c] Seyed Mehrdad Hosseini,[b] Eva Bittrich,[d] Julian Eliah Heger,[e] Pascal Kaienburg,[f] Subhrangsu Mukherjee,[g] Jiaying Wu, §[a] Moritz Riede,[f] Harald Ade,[g] Peter Müller-Buschbaum,[e] Martin Pfeiffer*[b] and James Robert Durrant *[ah]

Vacuum-processed organic solar cells (VP-OSCs) possess many advantages for scalability. However, as the academic community focusses on high performing solution-processed OSCs, detailed studies about the relation between morphology and device characteristics in VP-OSCs are rare. Here, we present a study on a model donor/fullerene VP-OSC system deposited at different substrate temperatures. Substrate heating results in increases in current density and fill factor (FF). Changes in morphology are characterised by grazing-incidence wide-angle scattering (GIWAXS) and resonant soft X-ray scattering (RSoXS). The increase in the degree of crystallinity and preferential orientation of the donor molecule in heated samples results in enhanced absorption increasing current density. The exciton and charge separation efficiency were studied by transient absorption and photoluminescence quenching and only showed minor differences. To study the FF differences, charge transport and non-geminate recombination are studied by optoelectronic measurements and device simulations. The charge carrier kinetics are governed by a large density of trap states. While the energetic disorder and non-geminate recombination under open circuit conditions remain largely unchanged, the increased effective mobility and lower transport disorder observed in photocurrent transients explain the increased collection efficiency for heated devices. We relate this to the increased donor phase purity. Our results suggest that charge recombination and transport are governed by different aspects of disorder related to amorphous and crystalline donor phases. Quantitative comparison with high FF solution-processed OSCs reveals that the low mobility limits FF. Finally, drift-diffusion simulations give an outlook for possible performance increases through further optimisation of the deposition control.

Received 13th August 2024,
Accepted 21st October 2024

DOI: 10.1039/d4ee03623a

rsc.li/ees

[a] *Department of Chemistry and Centre for Processable Electronics, Imperial College London, MSRH, 82 Wood Lane, London W12 0BZ, UK. E-mail: r.pacalaj18@imperial.ac.uk, j.durrant@imperial.ac.uk*
[b] *Heliatek GmbH, Treidlerstraße 3, 01139 Dresden, Germany. E-mail: martin.pfeiffer@heliatek.com*
[c] *Department of Engineering, Durham University, Lower Mount Joy, South Road, Durham DH1 3LE, UK*
[d] *Leibniz Institute of Polymer Research Dresden, Hohe Str. 6, 01069 Dresden, Germany*
[e] *Technical University of Munich, TUM School of Natural Sciences, Department of Physics, Chair for Functional Materials, James-Franck-Str. 1, 85748 Garching, Germany*
[f] *Clarendon Laboratory, Department of Physics, University of Oxford, Parks Road, Oxford OX1 3PU, UK*
[g] *Department of Physics, and Organic and Carbon Electronics Laboratory (ORaCEL), North Carolina State University, Raleigh, North Carolina 27695, USA*
[h] *SPECIFIC IKC, Faculty of Science and Engineering, Swansea University, Swansea SA2 7AX, UK*

† Electronic supplementary information (ESI) available: Including experimental details and additional supplementary results. See DOI: https://doi.org/10.1039/d4ee03623a

‡ Current address: Chemistry and Nanoscience Center, National Renewable Energy Laboratory, 15013 Denver West Parkway, Golden, CO 80401, USA.
§ Current address: Department of Chemical and Biological Engineering, Hong Kong University of Science and Technology, Room 6542, Academic Building, Clear Water Bay, Kowloon, Hong Kong.

Broader context

Lab-scale solution-processed organic solar cells (SP-OSCs) now achieve power conversion efficiencies in excess of 19%. Reproducibly translating this efficiency to large area modules, *i.e.* transitioning from spin-coating to scalable techniques, has proven difficult. Additionally, the stability of SP-OSCs remains an open issue. In contrast to that, vacuum-processing requires higher capital investment but has been proven to be scalable in the field of organic light emitting diodes. Vacuum-processing also allows for the scalable deposition of complex multi-junction and interlayer structures. Despite these advantages, the lab-scale efficiency of vacuum-processed organic solar cells (VP-OSCs) currently lags behind that of SP-OSCs. Due to the high required capex, only a few academic groups investigate the performance limitations of VP-OSCs and how they relate to material properties and the bulk-heterojunction performance. Here, we present a study combining detailed morphological and device characterisation. The morphology was varied through substrate heating during the deposition of the active layer. Our detailed study allows us to pinpoint device properties to characteristics of the active layer morphology. Additionally, the comparison with solution-processed references helps us to identify the VP-OSC performance bottlenecks. Our findings will be useful to guide materials and morphology optimisation to further increase the performance of scalable VP-OSCs.

1. Introduction

Vacuum-processed organic solar cells (VP-OSCs) exhibit a promising route to large scale commercialisation due to their intrinsic and morphological stability,[1] the synthetic simplicity and ease of purification of the utilised small molecule donors and fullerene acceptors,[2] and the scalable and high precision deposition methodology.[3] The industrial viability of thermally evaporating organic semiconductors has already been demonstrated for organic light emitting diode applications.[4] Industrial scale production of VP-OSCs has also been demonstrated – including bulk heterojunction (BHJ) active layers, complex interlayers and multi-junction structures with independently certified PV stability adhering to PV industry standards.[5,6] With regard to lab efficiencies, two-terminal multi-junction VP-OSCs reported by Heliatek GmbH have achieved a certified power conversion efficiency (PCE) of 13.2% in 2016 – an OSC efficiency record at the time.[4,5] However, single junction VP-OSCs remain limited to about 10% PCE.[7,8] In contrast, solution-processed single junction OSCs (SP-OSC) have achieved efficiencies up to 12% with fullerene acceptors[9,10] and most recently >19% with non-fullerene acceptors (NFAs).[11–15]

The high PCEs of SP-OSCs are motivation for extensive studies of their nanomorphology and charge carrier dynamics to guide further performance enhancements. In contrast, despite their commercial potential, there are relatively few studies of the underlying factors determining the PCE of VP-OSCs.[4] Herein, we focus on the correlation between nanomorphology and charge carrier dynamics in high performance BHJ VP-OSCs fabricated from a small molecule donor and C_{60} acceptor, and how these compare to SP-OSCs.

To date, the efficiency advances achieved with NFAs in SP-OSCs have not been mirrored in VP-OSCs. The highest performing single-junction VP-OSCs still rely on fullerene acceptors.[16] In part, this is due to the molecular size constraint imposed by thermal evaporation prohibiting the use of similarly large conjugated ring structures as present in the highest performing NFAs.[4,17] This difference in molecular size also plays a role in the aggregation behaviour of high performing solution *vs.* vacuum-processed BHJs and thereby impacts performance.[18]

High performance SP-OSC systems typically exhibit relatively ordered domains, with a composition of the mixed polymer-rich domains near the percolation threshold for electron transport and prevention of over-purification and excessive aggregation.[18–22] This has been shown to improve the charge generation and collection efficiency. Phase separation and purity can be aided through the use of solvent additives or post-deposition thermal/solvent-vapour annealing.[23–26] Evaporable small molecule donors paired with fullerene acceptors are believed to form intermixed blends, related to their similar size and stronger intermolecular interactions between donor and acceptor molecules.[18,27] Limited morphological optimisation for VP-OSCs[28] may be achieved through the use of templating substrates,[27,29] co-evaporants inducing crystallization,[30–33] thermal annealing[34,35] or by altering the substrate temperature during evaporation.[34,36–45]

It has previously been shown that vacuum-processed blends exhibit lower fill factors (FF) than efficient SP-OSCs.[17] This may originate from effects of field-dependent generation or charge collection. The former depends on the intrinsic energetic offset and excited state lifetimes as well as the morphology dependent contributions to these. Empirically, the latter has been inferred from the drop in FF typically observed for active layers thicker than 50 nm, thus limiting optical absorption and hence short-circuit current density (J_{SC}). In contrast, SP-OSCs typically achieve the highest performance at active layer thicknesses $\approx$100 nm,[46,47] indeed for some devices >300 nm.[20,48–52] A key challenge for VP-OSC is therefore gaining a better understanding of the interplay between deposition parameters, active layer morphology and the efficiency of charge separation, and collection (transport *vs.* non-geminate recombination) to maximise J_{SC} and FF.

Here, we present a study on the interplay between morphology, charge carrier dynamics and device performance for a VP-OSC model system: DCV-V-Fu-Ind-Fu-V:C_{60} (2 : 1)[53] that is structurally related to commercially relevant systems. The active layer morphology is altered by substrate heating during evaporation. This was empirically shown to improve the device performance in low performing planar[34,37,39–42] and bulk heterojunctions.[36,38,43–45] Few studies link the BHJ performance with film morphology (improved crystalline order and molecular orientation) but do not provide detailed device characterisation.[34,36] In this study we go beyond previous literature by combining detailed morphological and device characterisation in a relevant model blend.

We employ grazing-incidence wide-angle X-ray scattering (GIWAXS) and resonant soft X-ray scattering (RSoXS) to study substrate heating induced differences in molecular orientation and crystallinity, and the size and purity of phase-separated domains, respectively. Subsequently, we analyse the impact of the changed active layer morphology on solar cell operation – from charge generation (absorption, exciton quenching efficiency, charge separation) to charge collection (non-geminate recombination *vs.* charge extraction). Active layer films were characterised using UV/Vis absorption, photoluminescence quenching and ultra-fast transient absorption spectroscopy. To address the collection efficiency limitations, we employed transient photovoltage/photocurrent measurements and charge extraction analyses. We focus in particular on the impact of the energetic disorder in the blends that has been shown to strongly impact the FF of VP-OSCs.[54] Our analyses of the collection efficiency are compared to two SP-OSC references – employing small-molecule:fullerene (BTR:$PC_{70}BM$) and polymer:NFA (PM6:Y6) photoactive layers. Both of these solution processed references are known for their high collection efficiencies and thickness tolerance.[20,55–57]

We show that the increased crystallinity in films deposited on heated substrates explains the observed increases in photocurrent. While the non-geminate recombination is largely unaffected by the change in morphology, the increased effective mobility in the elevated temperature samples leads to an improved collection efficiency and thereby fill factor. The comparison with the solution-processed references reveals a strong carrier density dependence of the mobility and recombination rate constant in the VP-OSCs.[58–61] While recombination kinetics are comparatively slow in the VP-OSCs, the effective mobility is found to be the bottleneck compared to the SP-OSC references. Combining optoelectronic measurements and device simulations using the software package OghmaNano[62,63] we assign this to slow hole transport. Our morphological data suggests that substrate heating can partially mitigate this by increasing the donor crystallinity and phase purity leading to an increase in the effective mobility. We conclude by providing an outlook for possible performance increases for single junction VP-OSCs of DCV-V-Fu-Ind-Fu-V:C_{60} that could be achievable by further optimisation of the deposition control and/or adjustments of the molecular structure yielding improved donor aggregation.

2. Results

2.1 Materials, device architecture and performance

The structures of the evaporated donor and acceptor molecules, DCV-V-Fu-Ind-Fu-V and C_{60}, are shown in Fig. 1(a) (see ESI,† Fig. S1 for the structures of the SP-OSC reference materials BTR:PCBM and PM6:Y6, as well as device fabrication details). The DCV-V-Fu-Ind-Fu-V donor molecule is related to the more widely studied DCV5T-Me donor with A–D–A structure.[64] The BHJ was produced by co-evaporation in a 2:1 D–A-ratio by weight. During evaporation, the substrate was either kept at room temperature or heated to 50 °C (referred to as RT and 50 °C, respectively).

The active layer thickness of 50 nm was chosen as a compromise between absorption and charge carrier collection efficiency. While the optimum performance is achieved for thinner active layers, 50 nm also helps to reduce the impact of the device capacitance on optoelectronic measurements, as discussed in the methods section (see ESI†). The active layer is evaporated on a thin layer of undoped C_{60} and capped with undoped BPAPF (see ESI,† Fig. S1 for the structure), the electron and hole selective contacts, respectively. This interlayer structure minimises the effect of surface recombination of minority carriers at the contacts. An additional layer of n-doped C_{60} and p-doped BPAPF complete the respective interlayers. These aid the reduction of the series resistance by making the bulk of the transport layers more conductive.[65]

Fig. 1(b) shows a visual representation of the energy alignment of the device. Note that the offsets at the interfaces are not to scale. Further details about the device preparation can be found in the (ESI†). Fig. 1(c) shows the *JV*-curve of the RT and 50 °C device. Heating the substrate during evaporation yields an improved FF (61 *vs.* 53%) and J_{SC} (15.1 *vs.* 12.9 mA cm^{-2}) resulting in an improvement of the PCE from 5.8% to 7.9%. The V_{OC} of the 50 °C device only shows a small increase of about 10 mV compared to the RT device. This together with the very similar dark *JV*-curves shown in ESI,† Fig. S2 indicate similar voltage losses in the system.

ESI,† Fig. S3 shows the *JV*-curves of the SP-OSC references BTR:PCBM and PM6:Y6. The comparison illustrates the FF limitations of the VP-OSCs. The origin of the FF limitation, *i.e.*, field-dependent generation or charge collection, will be investigated in more detail below.

2.2 Identifying the main limitation from light intensity dependent *JV*-curves

To decouple the influence of different loss mechanisms on the device FF and J_{SC} discussed above, we first turn to the light intensity dependence of the device *JV*-parameters. Fig. 2(a)–(c) show the normalised *JV*-curves of the 50 °C and RT device, the BTR:PCBM reference and the PM6:Y6 reference, respectively. Around the maximum power point, a strong intensity dependence of the *JV*-curves indicates that the VP-OSCs are limited by the collection efficiency as the non-geminate recombination rate (recombination order >1) increases at higher generation rates. The evaporated devices exhibit an absolute loss in FF of more than 10% between 0.05 and 1 sun equivalent LED illumination, dominating the light intensity dependence of the PCE (see also Fig. 2(d) and (e)). In contrast, the SP-OSC references only show very little dependence of the FF and PCE on the light intensity. These data all indicate that the VP-OSCs, and particularly the RT device, exhibit less efficient charge collection than the SP-OSC references, despite their thinner, 50 nm photoactive layer thickness, compared to 100 nm for PM6:Y6 and 230 nm for BTR:PCBM.

At reverse and low forward bias, both VP-OSCs show very little variation in the normalised *JV*-curve shape with increasing light intensity. This is indicative of the *JV*-curves being dominated by a first order process rather than intensity dependent charge collection in this region. Efficient charge collection at

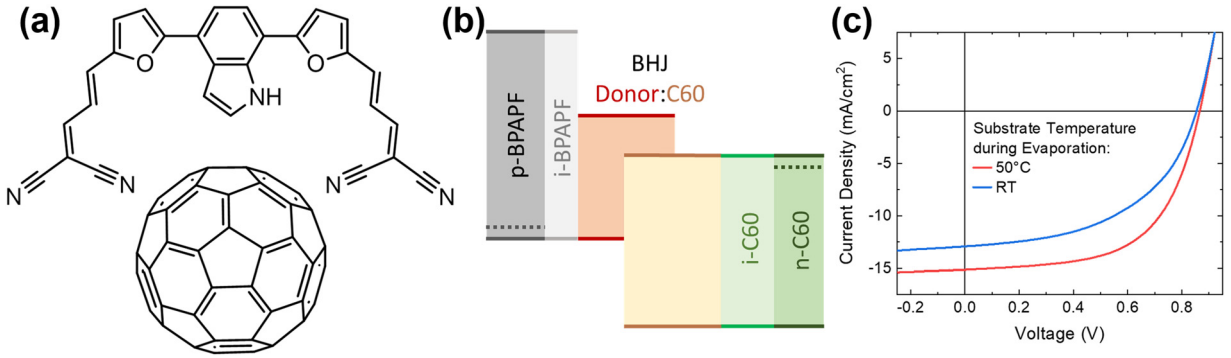

Fig. 1 (a) Chemical structure of the donor molecule DCV-V-Fu-Ind-Fu-V and the acceptor C_{60}. (b) Schematic of the relative energy levels of the active layer and interlayers. Note that the relative energetic alignment is deduced from a combination of literature and experimental values as described in the main text. (c) *JV*-curve of the devices with 50 nm active layer thickness used for the analysis herein.

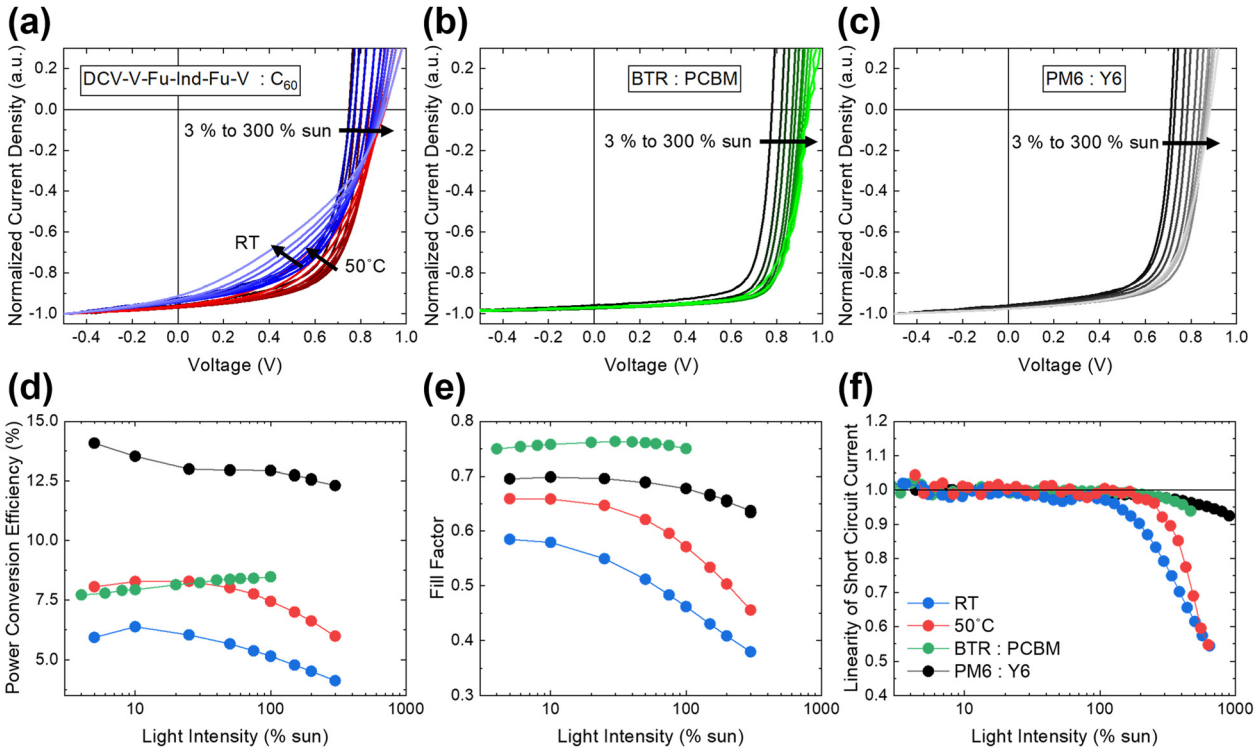

Fig. 2 (a)–(c) Normalised *JV*-curves of DCV-V-Fu-Ind-Fu-V: C_{60} (RT and 50 °C, blue and red, respectively), BTR:PCBM and PM6:Y6, respectively, for the range of 3% to 300% of 1 sun equivalent light intensity. (d)–(f) Light intensity dependence of power conversion efficiency, fill factor and linearity of the short circuit current density, respectively. See (f) for the legend.

J_{SC} up to 1 sun equivalent light irradiation is also demonstrated by the excellent J_{SC} linearity in Fig. 2(f). At light intensities above 1 sun, differences become discernible with a pronounced decrease in J_{SC} linearity of the VP-OSCs. The onset of the decrease occurs at lower light intensity for the RT *vs.* the 50 °C device (approximately 1 sun *vs.* 2 sun, respectively) in line with a reduced collection efficiency.

Given the good linearity up to 1 sun, the reduced J_{SC} in the RT device compared to that deposited at 50 °C (Fig. 1(c)) is more likely related to differences in absorption and field dependent geminate losses, as assessed below. The current saturation (ratio of J_{SC} to reverse bias current) of the 50 °C device around J_{SC} is improved and comparable with that of the non-fullerene reference, while the large offset fullerene reference (BTR:PCBM) shows the highest current saturation at J_{SC}.

These results indicate that the morphological modifications achieved by varying the substrate temperature during the evaporation process improve both the charge generation and collection elements of device function. While the charge collection is significantly improved in the 50 °C device, it still constitutes a performance bottleneck compared to the SP-OSC references. Following the in-depth assessment of the active

layer morphology, we will assess the charge generation, recombination and extraction in more detail.

2.3 Morphology analysis

Fig. 3(a) and (b) show the 2D GIWAXS data of the RT and 50 °C film, respectively. The 50 °C film has a strongly increased scattering intensity, indicating a significantly higher overall degree of crystallinity with preferential orientation. In Fig. 3(c), 1D diffraction patterns obtained from out-of-plane cake cuts of the RT and 50 °C films are shown against q. The reflexes located at (0.73 ± 0.01) Å^{-1} and (1.81 ± 0.01) Å^{-1} for the RT film are assigned to the (100) and (010) lattice planes of the orthorhombic unit cell, corresponding to lamellar and π–π-stacking, respectively, and shift to (0.77 ± 0.01) Å^{-1} and (1.86 ± 0.01) Å^{-1} for the 50 °C film. Hence, the corresponding lattice spacings d_{100} and d_{010} shift from (8.63 ± 0.05) Å to (8.18 ± 0.04) Å and from (3.47 ± 0.01) Å to (3.38 ± 0.01) Å, respectively, indicating a slightly denser molecular arrangement of the crystalline phase in the 50 °C film. Considering the lattice being formed by a stack of donor molecules, the (010) reflex is related to the π–π-stacking (*i.e.* face-on with respect to the substrate).[66] By comparison to similar GIWAXS patterns of vapour-deposited small organic molecular donors,[29,67,68] the (100) reflex can either resemble a tilted π–π-stacking of the molecule or stacking along the shortest axis (tilted or edge-on with respect to the substrate).

The full width at half maximum (FWHM) of the reflexes is a measure of the coherence length of the respective lattice planes (*hkl*), which is related to the crystallite size according to the Scherrer equation, where the size $L_{hkl} \sim 2\pi/\mathrm{FWHM}$.[69] Additional broadening effects due to the paracrystalline nature and lattice disorder of soft matter make a defined calculation of crystallite sizes non-trivial,[70] however, a qualitative estimation of their lower limit is possible. In ESI,† Fig. S4(c), the FWHM of the (010) reflex remains constant at (0.38 ± 0.01) Å^{-1}, while the FWHM of the (100) reflex narrows from (0.23 ± 0.01) Å^{-1} to (0.15 ± 0.01) Å^{-1} upon increasing the substrate temperature. This evolution suggests that the minimum crystallite size along the [010] direction remains constant, while it is 1.5 times larger along the [100] direction in the 50 °C film.

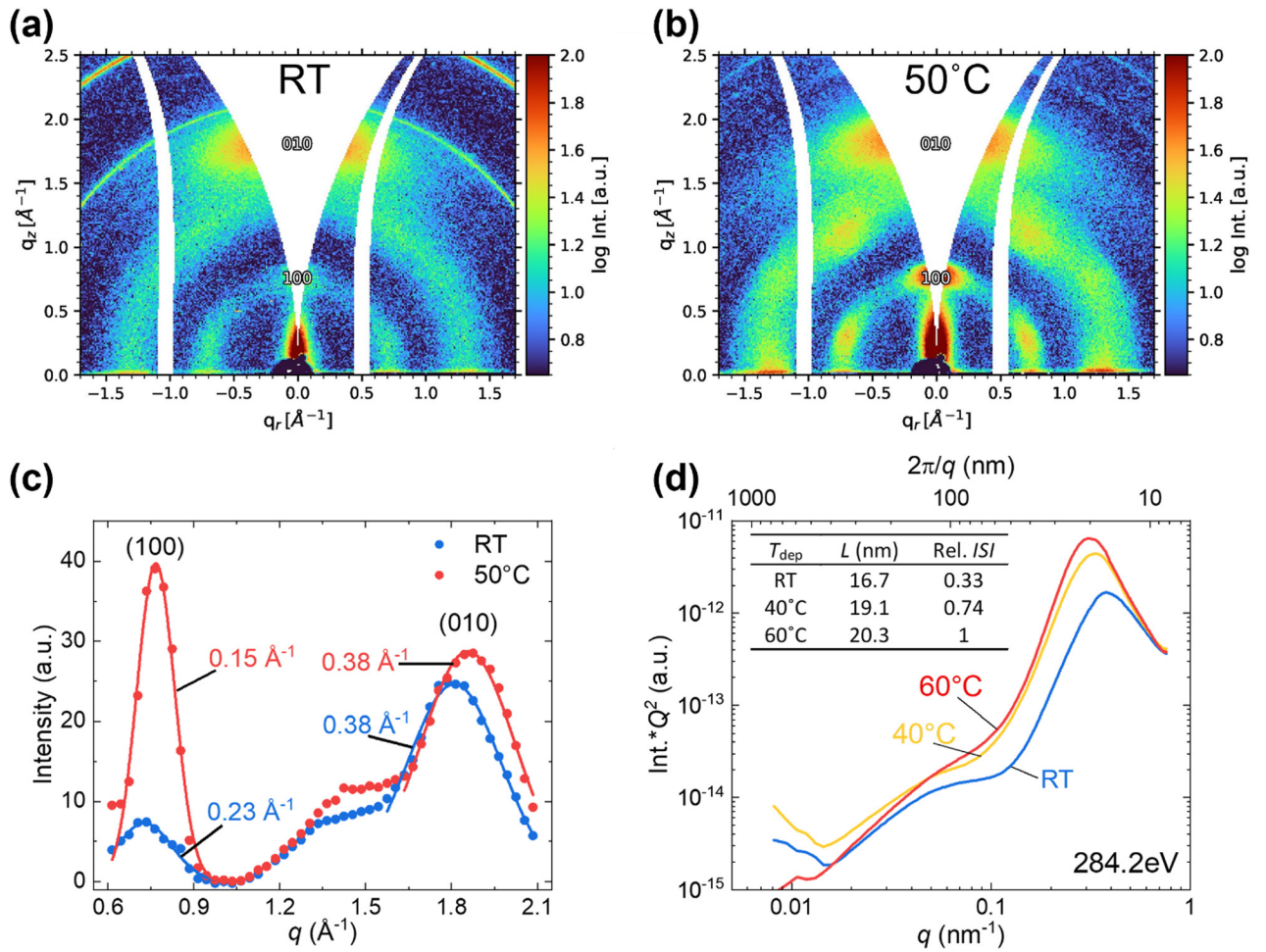

Fig. 3 (a) and (b) 2D-GIWAXS diffraction patterns for RT and 50 °C blend films, respectively. The sharp reflection in (a) is due to specular reflection from the edged Si substrate (see ESI,† Fig. S4). (c) 1D diffraction patterns obtained from out-of-plane cake cuts of the RT and 50 °C film, respectively. The Gaussian fits are shown in solid lines together with the corresponding FWHM values used to estimate the coherence length in the main text. (d) RSoXS data at resonance on a log–log scale for samples deposited at different substrate temperatures. The table indicates the long period L and integrated scattering intensity ISI normalized to the 60 °C sample.

Pole figures of radially integrated azimuthal tube cuts along the (100) reflex (ESI,† Fig. S4(d)) and the (010) reflex (ESI,† Fig. S4(e)) reveal the material quantity of crystallites in preferred orientation with respect to the substrate.[71] For both substrate temperatures, face-on and edge-on populations are observed. The results show a strongly increased preferential orientation for the (100) reflex in the 50 °C film judged by relative changes in scattering intensity, with about 3 times more crystallites in face-on orientation and about 8 times more in edge-on orientation, as compared to the RT film. When comparing the different preferential orientations for the (100) reflex, the amount of face-on orientation is about 12 times higher than edge-on orientation in the RT film, and about 5 times higher in the 50 °C film. The (010) reflex shows an about 1.3 times higher face-on orientation in the 50 °C film compared to the RT film. The increase in the (100) out-of-plane reflection indicative of an overall higher crystallinity is likely to increase the fraction of the integral transition dipole moment (expected to be parallel with the long molecular axis) within the substrate plane for the 50 °C film, thus enhancing the absorption of incident visible light within the photoactive blend, as we discuss further below.

Besides the average degree of crystallinity, the size of phase-separated domains and their purity are critical for BHJ device operation. Resonant Soft X-ray Scattering (RSoXS) is a technique capable of measuring the relative composition of domains as well as quantifying the size of the domains. The technique has previously been applied to SP-OSCs.[72–74] Fig. 3(d) shows blends deposited at different substrate temperatures (RT, 40 °C, 60 °C). The two slightly differing heated conditions were chosen in order to test the robustness of the established trend. Additionally, the donor content is slightly reduced to 60% from 66.7% (by weight).

The presence of a strong peak at $q \sim 0.3\ \mathrm{nm}^{-1}$ shows that phase separation occurs already at room temperature. With increasing substrate temperature, the long period L – indicative of the domain size – continuously increases from 16.7 nm at RT to 20.3 nm at 60 °C. These values are smaller than those typically obtained for SP-OSCs using the same technique.[26,75,76] The increase in domain size upon heating the substrate coincides with increased domain purity. This can be seen qualitatively by the higher RSoXS scattering intensity for higher temperature samples. When quantifying the relative domain composition with the relative integrated scattering intensity ISI,[73] the RT ISI is a third of the 60 °C sample. Note, that to be as close as possible to the device stack, the blends are sandwiched between layers of C_{60} and BPAPF which makes a quantitative interpretation of the ISI challenging. However, trends and the qualitative behaviour of the blends upon annealing can be deduced from the data as discussed alongside further details of the RSoXS measurements in ESI,† Fig. S5 and S6.

In summary, the RT sample already shows some degree of crystalline order and phase separation. Two populations of crystallites with edge-on and face-on orientation are observed. For the 50 °C sample, we observe an overall higher degree of crystallinity, tighter packing of molecules, larger crystallites in the lamellar direction and phase-separated domains becoming larger and purer. The crystallite size or disorder in π–π direction seems unchanged. Both orientation populations are also observed at 50 °C but the face-on orientation becomes more prevalent.

2.4 Charge generation: absorption, exciton dissociation and charge separation

To address the origin of the increased J_{SC} achieved through substrate heating, the optical properties of films with the two different active layer morphologies were studied. The neat donor DCV-V-Fu-Ind-Fu-V shows a high absorption coefficient similar to other small molecule donor (*e.g.* DCV5T-Me)[17,77] and NFA materials (*e.g.* Y6, ITIC)[57,78] with analogous A–D–A structures and di-cyano end groups. The absorption band of the donor in the region from 500 to 800 nm makes it a suitable candidate for a near infrared absorbing sub-cell. In blends, the 50 °C deposited films exhibit a stronger absorbance in the donor region compared to the RT films (Fig. 4(a)), indicating a better in-plane alignment of the donor transition dipole.

These observations agree with the GIWAXS data discussed above. The higher degree of order observed in the 50 °C film (increased crystallinity of edge-on and face-on phases) indicates that fewer molecules are tilted upwards towards an end-on

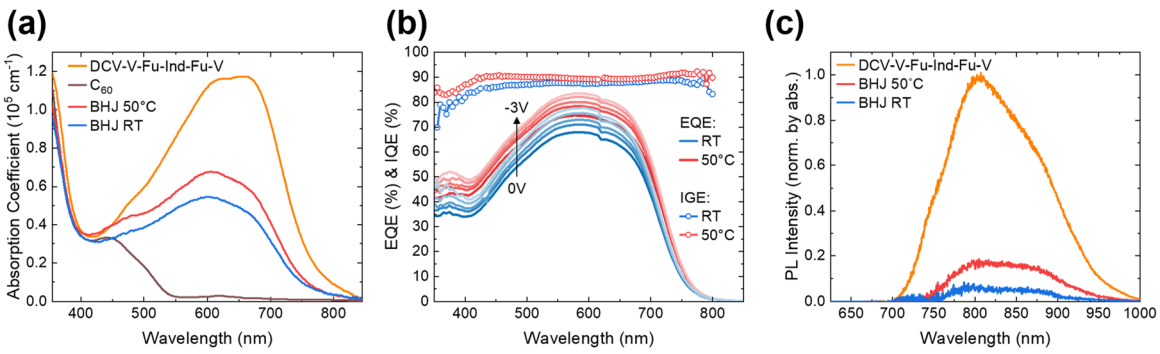

Fig. 4 (a) Absorption spectra of the neat donor DCV-V-Fu-Ind-Fu-V, acceptor C_{60} and blend films deposited at 50 °C and room temperature. (b) Field-dependent external quantum efficiency (EQE) spectra of the 50 °C and RT devices. Also shown is the internal generation efficiency (IGE) that was calculated as the ratio of the EQE at 0 V and −3 V. (c) Donor photoluminescence spectra of the neat donor, RT and 50 °C blends normalized by their absorption.

orientation, which is consistent with the increased optical absorption. Interestingly, the change in donor aggregation determined from the GIWAXS data does not lead to a significant shift in absorption, as observed in related DCV based small molecule donors (also see EQE absorption onset in ESI,† Fig. S7).[29,79] This would be in line with the presence of crystalline albeit smaller donor domains even in the RT films as also suggested by the morphological data.

The external quantum efficiency (EQE) data (Fig. 4(b)) indicate that the increase in film absorption observed for the 50 °C films is also reflected in an increase in photocurrent generation in complete devices. Measurements of the field dependent EQE were used to determine the quantum efficiency of charge separation by calculating the ratio of the EQE determined at 0 V and −3 V (Fig. 4(b)). It indicates a small improvement in the efficiency of charge separation for the 50 °C device, especially in the C_{60} absorption region. This is in line with the slightly improved saturation at reverse bias, as discussed above for the light intensity dependent *JV*-curves, most likely stemming from a small reduction in field dependent geminate recombination.

To assess the efficiency of exciton separation, the photoluminescence quenching efficiency (PLQE) of the BHJs was measured, as is commonly done for fullerene-based devices. Fig. 4(c) shows that the absorption corrected donor PL intensity is reduced by 86% and 96% in the 50 °C and RT blends respectively, relative to the neat donor film. Additionally, the exciton decay lifetime upon optically pumping the donor was measured *via* ultrafast transient absorption spectroscopy (see Fig. 5). The time resolved measurements show a reduction of the exciton lifetime (photo-induced absorption signal around 900 to 920 nm, see Fig. 5(a) and (b)) from ∼50 ps in the neat donor film to 2.9 ps and 1.9 ps for the 50 °C and RT films, respectively (see kinetic Fig. 5(c)). The fluence dependent kinetics of the blends as well as the neat donor lifetime and TAS spectra are available in ESI,† Fig. S8(a)–(f), respectively. Note, that the neat donor exciton lifetime was extracted as a weighted average of a biexponential decay with a significant slow decay phase. The reported value is significantly shorter than previously reported values for NFA materials.[80]

These exciton decay times are in good agreement with the observed trend of the PLQE. The lower PLQE and slower exciton decay observed for the 50 °C films are indicative of a less intermixed morphology, increasing the distance excitons must diffuse to reach a donor/acceptor interface,[81] in agreement with the GIWAXS (more crystalline) and RSoXS (larger and more pure domains) data discussed above. However, the effect of reduced exciton separation efficiency on current generation is compensated by the enhanced light absorption of the 50 °C device, consistent with its overall higher J_{SC}.

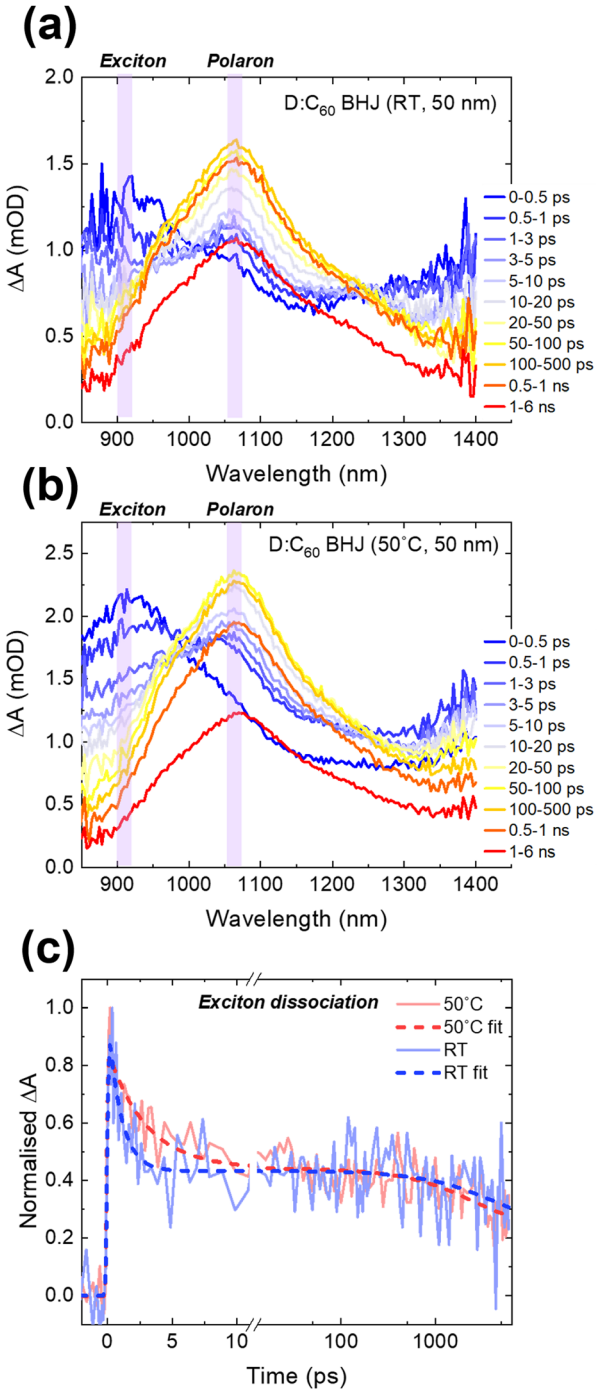

Fig. 5 (a) and (b) Transient absorption spectra of RT and 50 °C films, respectively, after selectively pumping the donor at 600 nm with a fluence of 6 μJ cm^{-2}. (c) Time evolution of the exciton signal between 900 and 920 nm together with fits of the exciton decay with lifetimes of 0.9 and 2.9 ps for RT and 50 °C, respectively.

2.5. Charge collection: disorder, non-geminate recombination and charge transport

As demonstrated above in Fig. 2, the dependence of the device FF upon light intensity indicates the FF of VP-OSCs studied herein is limited by carrier density dependent competition between non-geminate recombination and charge extraction. Both processes are known to be strongly impacted by the density of tail (shallow trap) states below the electronic gap of the bulk heterojunction.[55,82] We characterise the energetic disorder for the VP-OSCs as well as the SP-OSC references by measuring the total charge carrier density from differential capacitance (DC) *vs.* device V_{OC} as a function of light intensity,

following previously reported methodologies.[60,83–86] Despite the thin active layer thickness, the differential capacitance results in Fig. 6(a) demonstrate that the chemical capacitance can clearly be distinguished from the constant geometric capacitance for both VP-OSCs (see ESI,† Fig. S9 for the RT results). Over the measured range, the dependence of the chemical capacitance on the QFLS is well approximated by an exponential density of states with characteristic energy E_{ch}, as previously observed for a wide range of SP-OSC materials.

Fig. 6(b) shows the spatially averaged charge carrier density of the VP-OSCs and reference SP-OSCs plotted *vs.* the V_{OC} used as a proxy of the quasi-Fermi level splitting (QFLS). For better comparison of the slope of the tail state density against the solution processed references, the *x*-axis was offset by the V_{OC} at 2 sun equivalent illumination. Additionally, the ideal semiconductor charge density, with E_{ch} equal to the thermal energy, is shown.[87] The charge carrier densities and fitted E_{ch} values only show minor differences between the RT and 50 °C device. Characteristic energies, 53 and 50 meV for the RT and 50 °C devices respectively, are typical of many SP-OSCs[56,81] but significantly larger than the values obtained for BTR:PCBM (37 meV) and PM6:Y6 (31 meV). For BTR:PCBM and PM6:Y6, the low E_{ch} has been linked with their abilities to support efficient charge collection for thicker photoactive layers. Similar trends in CT state disorder have previously been observed in sensitive EQE measurements comparing PM6:Y6 and a range of VP-OSCs[88] while transport based techniques such as temperature dependent SCLC have yielded significantly different trends for the polaron disorder.[89] Below, high-resolution photocurrent transient and simulation results will be discussed that similarly yield different values of E_{ch}.

Transient photovoltage (TPV) was employed to determine the charge carrier recombination kinetics at the same open circuit and light bias conditions (up to 6 sun) as the differential capacitance results presented above. Based on the lifetimes τ and charge carrier densities n (see ESI,† Fig. S10 for τ *vs.* n), an effective bimolecular recombination coefficient can be calculated as $k_{BI} = (n\tau)^{-1}$.[90] The right axis of Fig. 6(c) shows the effective bimolecular recombination coefficient *vs.* the charge carrier density for the four devices studied. The 50 °C and RT device exhibit similar k_{BI}, with a slightly increased recombination rate observed for the 50 °C device. For the charge carrier density range characterised herein, both the VP-OSCs and the BTR:PCBM reference exhibit significantly slower recombination

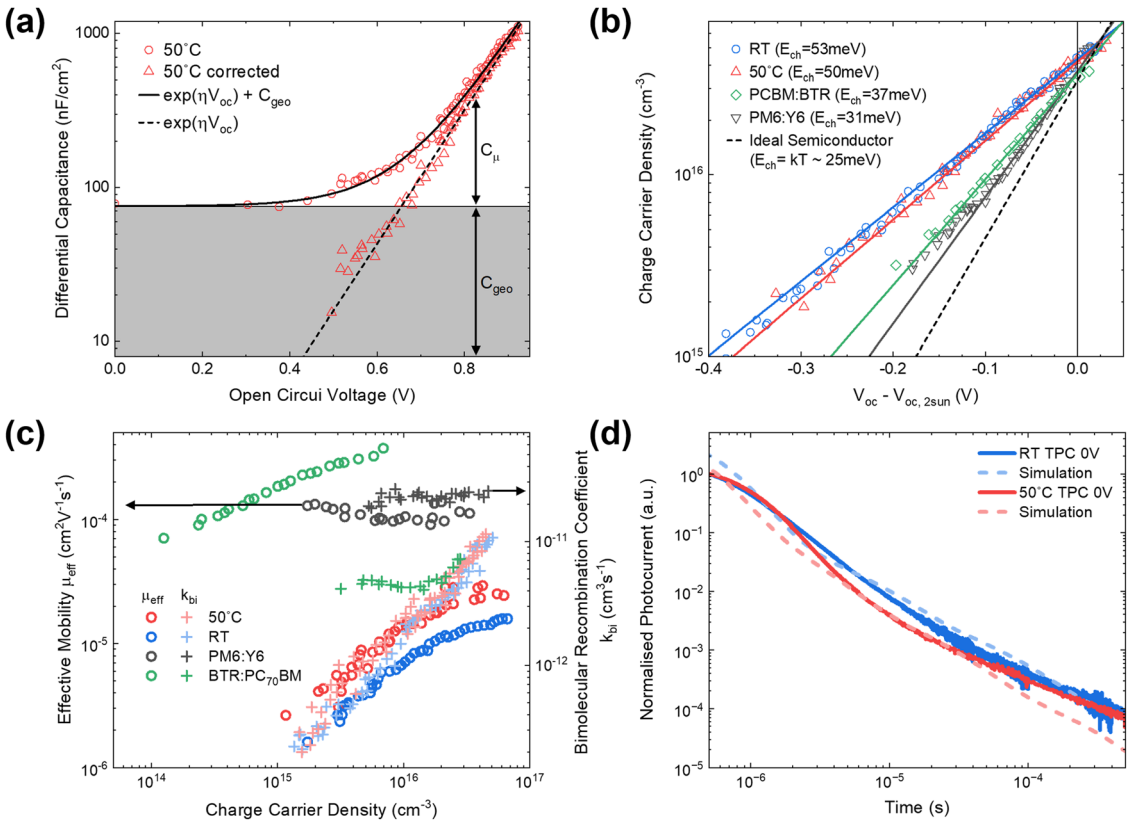

Fig. 6 (a) Differential capacitance *vs.* open circuit voltage (as measured and corrected for geometric capacitance) together with the respective fits for the 50 °C device. See ESI,† Fig. S9 for RT data. (b) Charge carrier density *vs.* the open circuit voltage referenced to the open circuit voltage at 2 sun equivalent illumination to enable a better comparison of the slopes. Exponential fits of the form $n_0 \exp(qV_{oc}/2E_{ch})$ and the bandtail of an ideal semiconductor are shown. (c) Effective mobility and effective bimolecular recombination coefficient *vs.* charge carrier density. Both axes scaled proportionally to each other to reveal the proportionality of the charge carrier dependence of mobility and recombination coefficient. (d) Normalised photocurrent transients measured using variable load resistances as described previously.[48,77] The dashed lines were simulated using OghmaNano using a global fit to experimental data as described below.

compared to PM6:Y6. For the SP-OSC references, the values are in excellent agreement with those determined by other methods such as bias assisted charge extraction (BACE) or photoinduced absorption (PIA).[89]

The solution-processed reference solar cells exhibit near ideal second order recombination kinetics as illustrated by the fitting of the lifetime *vs.* carrier density (see ESI,† Fig. S10) and the constant bimolecular recombination coefficient (Fig. 6(c)). The VP-OSC devices exhibit non-ideal (apparent third order) recombination and consequently a charge carrier density dependent k_{BI}, attributed to their higher energetic disorder.[86] To verify the validity of the analyses, the V_{OC} was reconstructed using the lifetime and carrier density data as well as J_{SC} as a proxy for the generation current. An excellent agreement is obtained between the measured and reconstructed V_{OC}, as shown in ESI,† Fig. S11, highlighting the reliability of the charge carrier density and lifetime data.

Following the assessment of the recombination kinetics, we turn to measurements of the effective charge carrier mobility (μ_{eff}). The effective mobility was assessed by measuring the charge carrier density accumulated in the device under short circuit conditions with varying background light intensities.[91] This method yields a charge carrier density dependent effective mobility dominated by the slower carrier type that has been shown to determine the electronic quality and FF.[92] This method was chosen as it can be performed on devices under operating conditions (without the need for different interlayers as in single carrier devices) and under realistic charge carrier densities.[93,94] The resulting values of the charge carrier density dependent mobility are plotted on the left axis of Fig. 6(c). The mobility of the 50 °C device shows an improvement by a factor of two relative to the RT device across the whole range of the measured charge carrier density. Given their similar recombination coefficients, this increase in mobility explains the increased FF of the 50 °C device, as we discuss further below. As both *y*-axes are plotted proportionally to each other, it is possible to directly compare the charge carrier dependence of both μ_{eff} and the k_{BI}. Both VP-OSCs show a strong charge carrier dependence in μ_{eff} similar to the k_{BI} at low charge carrier densities. BTR:PCBM shows only a weak carrier density dependence while PM6:Y6 shows virtually no carrier density dependence of the mobility, consistent with the lower energetic disorder and the absence of trap filling effects.

ESI,† Fig. S12 shows normalised photocurrent transients; these were used to determine the charge density in the devices at short circuit. The faster current transients of the SP-OSC devices qualitatively indicate a higher mobility in these blends (ESI,† Fig. S12(e)), consistent with Fig. 6(c). The strong biphasic character observed for the VP-OSC devices has previously been related to slow extraction from deeper trap states in evaporated bulk heterojunctions, most pronounced at low light intensity (see ESI,† Fig. S12).[35] High resolution transient photocurrent measurements have previously also been used to quantitively assess the characteristic energy.[62,95,96] Fig. 6(d) shows the high resolution current transients measured with variable load resistances for the RT and 50 °C devices. In contrast with the energetic disorder derived from the carrier density *vs.* V_{OC}, these transport-based measurements combined with a global fit of the optoelectronic data using drift-diffusion simulations (OghmaNano) indicate higher values of E_{ch}. A global fit of all data results in values of 121 meV and 89 meV for the RT and 50 °C devices, respectively, contrasting the lower values of characteristic energy determined from measurements at open circuit (53 meV and 50 meV, respectively). We therefore assign the improved FF in the 50 °C device to the overall increased effective mobility and a reduction in the transport related disorder as observed in these current transients. At the same time, the non-geminate recombination kinetics are similar for both VP-OSCs and comparatively slow compared to the SP-OSC references. The different magnitudes of energetic disorder from our open circuit charge extraction measurements (Fig. 6(b)) and short circuit photocurrent transient (Fig. 6(d)) analyses are discussed below.

3. Discussion

To summarize our results on the difference in charge generation between the RT and 50 °C devices, we can conclude that heating the substrate during evaporation results in a preferential molecular alignment which increases light absorption (Fig. 4(a)), resulting in the observed enhanced J_{SC}. The small reduction in the field-dependence of charge separation inferred from the field-dependent EQE (Fig. 4(b)) is in line with the improved saturation observed in the *JV*-curves of the 50 °C device. Such observations have previously been linked to an increase in phase purity and crystallinity aiding charge delocalisation or providing an energetic gradient through changes in the fullerene electron affinity.[97–100] This is in line with the morphological data presented herein. The increase in absorption and suppressed geminate recombination outweigh the small reduction in exciton separation efficiency observed for the larger phase-separated domains in the 50 °C device through PLQE and ultrafast exciton dynamics data (Fig. 4(c) and 5).

Both VP-OSCs studied herein exhibit an absorption onset around 800 nm (E_g = 1.72 eV) together with a V_{OC} of around 0.85 V. This voltage loss compares unfavourably with PM6:Y6 which exhibits a similar V_{OC} at a much smaller optical bandgap of 930 nm (E_g = 1.33 eV). It is however more comparable to typical voltage losses observed for SP-OSCs employing fullerene based acceptors including BTR:PCBM (E_g = 1.92, V_{OC} = 0.90 V), attributed at least in part to a larger energetic offset requirement for efficient exciton separation with fullerene acceptors.[16,101–103] Besides this limitation posed by the persistent use of fullerene acceptors in high performance VP-OSCs, the main performance limitation arises from the poor charge collection efficiency limiting the device FF even in 50 nm thin devices as illustrated in Fig. 2.

3.1 Quantifying the collection efficiency

In the literature, several figures of merit are generally connected to the collection efficiency and FF of OSC devices. The main difference between these is the weighting of the mobility and bimolecular recombination coefficients. In the simplest

case of the Langevin reduction factor ($\gamma \propto \mu/k_{BI}$)[89] or mobility-lifetime product, both mobility and recombination rate constant are given an equal weighting. Bartesaghi *et al.* derived a collection efficiency term $\theta \propto \mu^2/k_{BI}$ with different weighting of mobility and recombination rate constants.[104] This has been further improved by Kaienburg *et al.* to account for other effects such as the influence of imbalanced mobilities, yielding an electronic quality factor $Q = \mu^2/k_{BI}$[0.8, 92].

Table 1 lists the values of the effective mobility, calculated Langevin recombination coefficient, experimental bimolecular recombination coefficient as well as the Langevin reduction factor and electronic quality Q determined at a charge carrier density corresponding to MPP under 1 sun equivalent illumination (see the caption of ESI,† Fig. S13 for details about the calculation). Additionally, Q_{JV} was calculated directly from the *JV*-data using the equation provided by Kaienburg *et al.* reproducing the trends of the experimental values. The value of Q obtained for the RT device is comparable to those reported for similar donor molecules such as the DCV5T-Me:C_{60} blend.[17] While it is improved 3–4 fold in the 50 °C device to values of 0.53 and 0.39 for Q_{Exp} and Q_{JV}, respectively, more crystalline blends like ZnPc:C_{60} achieve values in excess of 1.[17] The values determined herein for the SP-OSCs are within the range reported previously. BTR:PCBM stands out, highlighting the superior electronic quality of some fullerene-based devices even compared to high performing NFAs.[17,92]

Since the mobility and bimolecular recombination coefficient are strongly charge density dependent in the evaporated cells, Q, k_L and γ also vary with light intensity (see ESI,† Fig. S13 for the light intensity dependence of Q_{Exp}, Q_{JV} and γ). Comparison with a single value of γ, as often quoted in the literature, may therefore be misleading, especially if it is based on a value of k_L calculated from SCLC mobilities determined at higher charge carrier densities unrepresentative of 1 sun operating conditions. It is evident from Table 1 that the Langevin reduction factors of the PM6:Y6 and the 50 °C devices are similar at 1 sun, and therefore that this Langevin based analysis is insufficient to explain the greater charge collection and FF limitations of the 50 °C device. By giving a higher weighting to the mobility, the electronic quality Q_{Exp} proves to be a more suitable measure to explain the FF variations. The similarity between the values obtained from transient optoelectronic experiments and those directly calculated from the *JV*s highlight the potential of Q_{JV} as a screening tool.

3.2 Recombination mechanism and drift-diffusion simulation

Previous studies have correlated strong charge carrier density dependencies of charge mobilities and effective recombination rate constants, as observed herein for our VP-OSCs, with the presence of energetic disorder.[60,61,86,91] Energetic disorder will lead to large populations of shallowly trapped electrons and holes, the density and energetic distribution of which will be strongly dependent on the applied voltage and light intensity. The effective hole and electron mobilities will depend on the mobility of free carriers as well as the fraction of trapped carriers. Similarly, recombination in the presence of a large density of sub-gap traps can be described as free electrons (holes) recombining with trapped holes (electrons) as well as free-to-free recombination. As the charge carrier density increases, the relative contribution of these channels to the overall recombination flux changes, leading to deviations from ideal second order kinetics.[61]

The presence of energetic disorder can often lead to discrepancies in experimentally determined charge carrier lifetime data, depending on the charge carrier density regime these were measured at.[105] To illustrate this, we used the fluence dependent decay of the polaron signal in the transient absorption measurements (see ESI,† Fig. S8) to calculate the k_{BI}. An estimate of the charge carrier density excited by the laser pulse was calculated from the device EQE at the excitation wavelength. Fig. 7 shows the results of the calculation side by side with the values obtained by the combination of TPV and DC measurements.

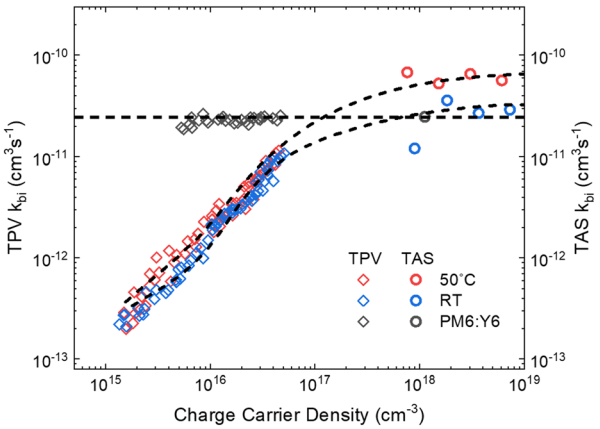

Fig. 7 Bimolecular recombination coefficients of PM6:Y6, the RT and 50 °C device measured by transient photovoltage/differential capacitance and transient absorption spectroscopy. For PM6:Y6 the dashed line is a guide to the eye demonstrating the good agreement of the values obtained with both methods. For the RT and 50 °C device, the dashed lines are based on OghmaNano simulations with an additional recombination coefficient for free electron to free hole recombination set to match the k_{BI} value obtained from the transient absorption measurements.

Table 1 Effective mobility (μ_{eff}), Langevin recombination coefficient (k_L), measured effective bimolecular recombination coefficient (k_{BI}), Langevin reduction factor (γ) and electronic quality (Q_{Exp}) assessed at a charge carrier density corresponding to MPP conditions at 1 sun illumination. Additionally, the electronic quality determined from the 1 sun *JV*-curve (Q_{JV}) is listed

Material	μ_{eff} [$cm^2\ V^{-1}\ s^{-1}$]	k_L [$cm^3\ s^{-1}$]	k_{BI} [$cm^3\ s^{-1}$]	γ	Q_{Exp} [$cm^{1.6}\ V^{-2}\ s^{1.2}$]	Q_{JV} [$cm^{1.6}\ V^{-2}\ s^{1.2}$]
DCV-V-Fu-Ind-Fu-V:C_{60} (*RT*)	1.2×10^{-5}	6.1×10^{-12}	4.3×10^{-12}	1.4	0.18	0.10
DCV-V-Fu-Ind-Fu-V:C_{60} (50 °C)	2.0×10^{-5}	1.1×10^{-11}	4.1×10^{-12}	2.6	0.53	0.39
BTR:PCBM	3.5×10^{-4}	1.8×10^{-10}	4.5×10^{-12}	40	142	819
PM6:Y6	1.2×10^{-4}	6.4×10^{-11}	2.3×10^{-11}	2.8	5.0	23.3

It is apparent that the optoelectronic measurements are conducted at light intensities relevant to solar irradiation conditions, while the pump pulses used for transient absorption measurements generate orders of magnitude higher charge carrier densities. In the case of charge carrier density dependent bimolecular recombination coefficients – as observed previously for fullerene based SP-OSCs[84,106,107] as well as the VP-OSCs studied herein – this will lead to discrepancies between high-fluence TAS and comparatively low light intensity optoelectronic measurements. Here, it allows us to show that the k_{BI} saturates above a carrier density of 10^{18} cm^{-3} for the VP-OSCs. Such a behaviour was previously reported in the literature for fullerene based SP-OSCs and may be related to the saturation of trap states and the more dominant role of free-to-free recombination.[106] While the recombination kinetics at irradiation levels relevant to device operation were similar, the 50 °C device shows a two-fold increased saturated k_{BI} of about 6×10^{11} cm^3 s^{-1}. Both saturated values exceed the value obtained for the PM6:Y6 reference. It is also striking that for PM6:Y6, we obtain good agreement between the k_{BI} determined from TAS and TPV/CE studies, consistent with greatly suppressed energetic disorder in this device and near ideal bimolecular kinetics.

To investigate the contribution of the different recombination channels in more detail as well as shed light on the origin of the slow phase observed in current transients, we employed the simulation software OghmaNano. The software treats intra-gap trap states as an ensemble of trap states with discrete energy levels making up an exponential tail and solving the trapping and recombination rate equations for every trap level independently.[62] The simulation parameters shown in ESI,† Table S1 were extracted by performing a global fit to light and dark *JV*-curves, the 1 sun TPV transient, high resolution photocurrent transients at variable bias (−1 V, 0 V, 0.5 V) as well as V_{OC}, J_{SC} and *n vs.* light intensity (see ESI,† Fig. S14 and S15).

The charge carrier lifetimes and effective mobility were extracted from the simulations and compared to the values determined experimentally (see ESI,† Fig. S16). The good agreement in the general trends and the small deviation in absolute values within a factor of two indicate the overall applicability of the model to the devices studied herein. We note that, no free-electron-to-free-hole recombination channel was necessary to reproduce the optoelectronic experimental results. However, at the much higher fluences experienced by the device in a TAS experiment, an additional direct free-to-free recombination channel ($k_{free\text{-}to\text{-}free}$ of 6.6×10^{-11} and 3.3×10^{-11} cm^3 s^{-1} for 50 °C and RT, respectively) was needed to reproduce the higher light intensity trends (see dashed lines in Fig. 7) in line with a pronounced contribution of free carrier recombination.

While the experimental data of the 50 °C device can be accurately reproduced using symmetric trap populations (symmetric hole and electron E_{ch} and trap densities), the global fit to the RT data required an asymmetry of the trap density and larger E_{ch} (121 meV *vs.* 89 meV for RT and 50 °C, respectively). These values of the characteristic energy that are primarily determined from the fitting of the photocurrent transients differ significantly from the values obtained for the combined tailslopes determined from charge density measurements *vs.* V_{OC} (53 meV and 50 meV for RT and 50 °C, respectively). The latter together with lifetime data from TPV was used to accurately reconstruct the experimentally determined V_{OC} including their ideality, as shown in ESI,† Fig. S11. This indicates that the disorder obtained from charge extraction measurements determines non-geminate recombination at open circuit conditions ($n > 10^{15}$ cm^{-3}) while the photocurrent transients may be governed by energetically lower lying traps and asymmetric populations.

Potentially in line with this observation, Saladina *et al.* recently reported a power law DoS in DCV-V-Fu-Ind-Fu-V:C_{60}. They inferred this from light and temperature dependent ideality factors.[53] A consequence of their observations would be a narrower DoS compared to an exponential bandtail but with an increasing breadth of states (increasing E_{ch}) deeper into the bandgap. Qualitatively this may be similar to our observations of a larger E_{ch} fitted to the slow phase of current transients corresponding to states deeper in the gap and asymmetric bandtails. Another possible explanation for asymmetric transport properties affecting the photocurrent transients may be the increased presence of spatially isolated donor domains in the RT film as supported by the lower phase purity and smaller domain size shown in RSoXS and GIWAXS data, respectively. While contributing to non-geminate recombination, these domains may slow down charge extraction as holes have to travel through amorphous and intermixed regions leading to the observed disorder in current transients and the asymmetry of the hole and electron density that was necessary to achieve a good global fit. In support of this observation, ESI,† Fig. S17 illustrates that a reduction in donor content leading to less aggregated donor phases results in a similarly pronounced slow phase of the current transient as observed in the RT device. Charge transport between isolated donor domains *via* tunnelling or hole transport through C_{60} has previously been linked to slow current transients.[108] The polaron disorder in amorphous phases has previously been established as a key determinant of hole mobility in small molecule hole transport materials.[109,110]

Our observations may also point to fundamental discrepancies in the determination of disorder through transport-based techniques (current transients, temperature dependent SCLC), techniques relating charge accumulation and QFLS (impedance spectroscopy, charge extraction *vs.* V_{OC}, V_{OC} ideality), and techniques based on the fitting of CT state emission/absorption. These have previously yielded a wide range of disorder parameters and even differ in the DoS shape (Gaussian *vs.* exponential *vs.* power law).[53–56,87–89] A full discussion of the different techniques and results is however beyond the scope of this study.

In summary, charge carrier build-up and recombination under open circuit conditions are largely unaffected by the change in substrate temperature during deposition. Both are characterised by a broad distribution of tailstates compared to PM6:Y6 and BTR:PCBM but comparable to other SP-OSC materials as measured by the same methodology. Simulation results

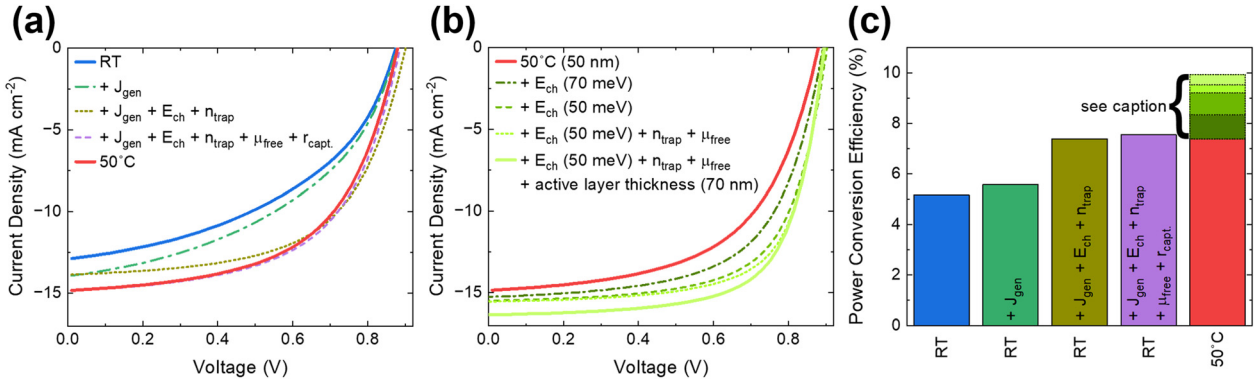

Fig. 8 (a) Simulated fitted *JV*-curves of the RT and 50 °C device. Additionally shown are the *JV*-curves for the RT device with iteratively changing the generation current (J_{gen}), the trap symmetry and density (n_{trap}), and the mobility of carriers at the band edge (μ_{free}) and the capture cross-section of the charge carriers ($r_{capture}$) to the values obtained from the global fit of the 50 °C device. (b) Simulated *JV*-curves visualising the effect of adjusting E_{ch}, free mobility, trap density and active layer thickness to achieve 10% PCE. (c) PCE corresponding to the simulated *JV*-curves in (a) and (b). Improvements beyond the performance of the 50 °C device parameter changes described in the legend of (b). The full list of modelling parameters can be found in ESI,† Table S1.

consistently explain the observed charge carrier density dependence of the effective recombination coefficient and mobility through a recombination formalism involving trapped and free carriers. Our results show that while the non-geminate recombination rate at operational charge carrier densities is sufficiently slow compared to the SP-OSC references ($\sim 4 \times 10^{-12}$ cm^3 s^{-1}), the observed low collection efficiency and FF can be rationalized by the overall low mobility ($\sim 10^{-5}$ cm^2 V^{-1} s^{-1}), likely resulting from large energetic disorder during charge transport. Depositing at higher substrate temperatures induces favourable changes in microstructure, improving structural order and phase separation, which goes along with improved energetic disorder for charge transport and a twofold increase in effective mobility. In the following, we explore the gains in single-junction device performance that would result from further improving morphology, disorder and charge carrier dynamics.

3.3 Performance prospects of VP-OSCs

To deconvolute the influence of the different simulation parameters on the *JV*-curves and performance of the devices, we adjusted the parameters of the RT device iteratively until reproducing the 50 °C parameters (see Fig. 8(a) and (c)). The plot indicates that the trap density and the characteristic energy dominate the observed changes in FF and PCE while the increased free mobility values and trapping/recombination capture cross-sections only result in a small reduction of V_{OC} due to the slightly increased recombination rate, while J_{SC} and FF increase due to better charge collection. Using the OghmaNano drift-diffusion model, we further explored what improvements in device parameters would lead to a PCE of 10% in a single junction device using DCV-V-Fu-Ind-Fu-V:C_{60} as the photoactive layer. Note that in practice, this blend may be used as a near-infrared absorbing sub-cell in a multilayer stack to achieve broadband absorption and minimise thermalisation losses, and thereby boost performance.[111–113]

Further reducing transport E_{ch} to 50 meV yields a large improvement in FF.[54] Comparatively, the influence of halving the trap density and an increased free mobility yields only small further improvements (see ESI,† Table S1 for the full list of simulation parameters). This reduction in the energetic disorder improves the collection efficiency and allows for the active layer thickness to be increased to 70 nm. At 70 nm the absorption of the active layer reaches its first interference maximum leading to an improved J_{SC} outweighing the reduction in FF (see ESI,† Fig. S18 for transfer matrix simulations). Note that in VP-OSCs the inclusion of doped transport layers as optical spacers can shift the interference maxima and further improve absorption.[17,111,114] This demonstrates the potential that lies in improving the collection efficiency through morphological and structural modifications of existing high-performance systems.

To close the efficiency gap with SP-OSCs, single-junction VP-OSCs will furthermore require a reduction in the voltage losses related to the D/A energy offset required for efficient charge generation as demonstrated for modern NFAs in SP-OSCs. Achieving high generation efficiency at low offsets may also require an increased exciton lifetime of the donor materials.[80,115] Kaienburg *et al.* demonstrated that in principle evaporable donor molecules may achieve reduced voltage losses when paired with the NFA Y6 in hybrid devices where the donor is evaporated onto the solution-processed NFA.[16] While the introduction of evaporable NFAs may allow for better energy level tuning, it remains to be seen whether charge generation properties of solution-processed acceptors like Y6 can be mirrored in smaller molecules suitable for evaporation. Additionally, our results show that despite the lower C_{60} content by weight, the electron mobility is not limiting performance. The use of evaporable NFAs may have detrimental effects on charge collection due to the anisotropy of planar molecules and likely intermixed blend morphologies. Therefore, potential high-performance evaporable NFAs should exhibit high mobilities and sufficiently phase separated blends to ensure good charge transport through the respective crystalline phases. A particular focus should therefore lie on optimising the interaction parameters and miscibility of the similarly sized evaporable donor and

NFA molecules[116,117] as well as the optimisation of deposition parameters.

4. Conclusions and outlook

Morphological optimisation through substrate heating during the vapour deposition of organic solar cells made from the model material combination DCV-V-Fu-Ind-Fu-V:C_{60} was shown to greatly improve the device performance. Absorption spectroscopy and GIWAXS measurements revealed that the origin of the improved J_{SC} lies in the improved crystallinity and preferential orientation of the donor's transition dipole parallel to the substrate for films deposited at 50 °C rather than room temperature.

Substrate heating also led to a substantial increase in FF. To investigate this, we determined the non-geminate recombination rate constants and effective mobility. Both are highly charge density dependent which is characteristic of charge carrier dynamics in the presence of a high trap density. The origin of the FF improvement lies in the two-fold increase of the effective mobility related to the reduction in energetic disorder and deep lying tailstates inhibiting charge transport. At the same time, recombination kinetics remained largely unaffected under operational conditions. The reduced mobility and the slow phase in current transients are tentatively assigned to amorphous/spatially isolated donor phases that trap holes. This is further supported by the RSoXS measurements that indicate a higher phase purity for films deposited at elevated substrate temperatures.

Our morphological data together with the optical and optoelectronic characterisations suggest that the phase purity and the decrease in amorphous phase size are key to reducing the disorder related to charge transport that limits the device FF. Further increasing the substrate temperature during evaporation may increase the size of crystalline domains leading to further reduction of the exciton quenching efficiency or cause changes in the molecular orientation resulting in a loss in absorption.[110] Due to the large anisotropy of the small molecule blends, our results demonstrate that morphological optimisation of evaporated organic solar cells is non-trivial but may enable large performance increases.

Simulations revealed that the reduction in intra-gap states, without negatively affecting other aspects of device performance, could lead to further significant performance increases in this evaporated model system beyond 10% PCE for single junction devices. This requires careful morphological optimisation and may further be aided by modifications of the molecular structure that could aid aggregation *e.g.* steric groups that have been shown to affect morphology in blends.[64]

Further improvements in single-junction efficiency will require a reduction of the voltage losses resulting from the trade-off between the energy level offset and efficient charge generation by addressing the relatively short exciton lifetime.[80] Evaporable NFAs may provide an avenue to reducing voltage losses.[16] When replacing fullerenes with NFAs, good electron mobility and sufficient phase separation in blends with similarly sized donors will be key to achieving good collection efficiency and overall performance.

Boosting the single-junction efficiency of vacuum-processed solar cells will translate to improved multi-junction efficiencies and further raise the prospects of their large-scale commercialisation.

Author contributions

R. A. P. wrote the manuscript and carried out the *JV*-characterisation, steady-state optical measurements and transient optoelectronic measurements as well as assisting with device simulations in OghmaNano. Y. D. measured and analyzed transient absorption spectroscopy measurements. R. C. I. M. carried out the global fit to the experimental data and device simulations. J. E. H. and E. B. provided the GIWAXS measurements and together with P. M.-B. analyzed their results. P. K. measured RSoXS data with support by S. M. and H. A. in the interpretation of the data. I. R., S. M. H. and M. P. planned experiments and provided invaluable information for the interpretation of results. J. W. provided additional optoelectronic data for reference devices. J. R. D. supervised the project. All authors contributed to the manuscript through discussions and useful feedback.

Data availability

The data supporting this article have been included as part of the ESI.†

Conflicts of interest

M. P. is co-founder and employee and S. M. H. is employee of Heliatek GmbH. M. R. is founder of TerraChange Solar Ltd.

Acknowledgements

We gratefully acknowledge Heliatek GmbH and in particular Dr Marieta Levichkova for supplying the tested samples and useful discussions. We would further like to thank Dr Tack-Ho Lee for supplying solution processed reference devices and Dr Weidong Xu for help with the collection of the photoluminescence spectra. R. A. P., Y. D. and J. R. D. would further like to acknowledge the financial support from the EPSRC (project ATIP EP/T028513/1 and Plastic Electronics CDT, EP/L016702/1). R. A. P. would further like to acknowledge the Korean NRF GRL project (NRF-2017K1A1A2013153). P. K. acknowledges financial support from the EPSRC (EP/V035770/1) for his Postdoctoral Fellowship and David Clarke Fellowship and further wishes to thank Linacre College for the award of a Junior Research Fellowship. The work at NCSU was supported by the Office of Naval Research (N000142012155 and N000142412104) and Goodnight Foundation Endowment. J. E. H. and P. M.-B. acknowledge funding from Deutsche Forschungsgemeinschaft (DFG, German Research Foundation) under Germany's Excellence Strategy – EXC 2089/1 – 390776260 (e-conversion) and by

the Bavarian State Ministry of Science, Research, and Arts in the context of the Bavarian Collaborative Research Project Solar Technologies Go Hybrid (SolTech). E. B. acknowledges funding by the Saxon State Ministry of Science and Art within the project STEEP UP. The project was selected in the Joint Transnational Call 2022 of M-ERA.NET 3, an EU-funded network of about 49 funding organisations (Horizon 2020 grant agreement no. 958174).

References

1 Q. Burlingame, X. Huang, X. Liu, C. Jeong, C. Coburn and S. R. Forrest, Intrinsically stable organic solar cells under high-intensity illumination, *Nature*, 2019, **573**, 394–397.
2 A. Mishra and P. Bäuerle, Small Molecule Organic Semiconductors on the Move: Promises for Future Solar Energy Technology, *Angew. Chem., Int. Ed.*, 2012, **51**, 2020–2067.
3 B. Qu and S. R. Forrest, Continuous roll-to-roll fabrication of organic photovoltaic cells via interconnected high-vacuum and low-pressure organic vapor phase deposition systems, *Appl. Phys. Lett.*, 2018, **113**, 053302.
4 M. Riede, D. Spoltore and K. Leo, Organic Solar Cells—The Path to Commercial Success, *Adv. Energy Mater.*, 2021, **11**, 2002653.
5 C. Uhrich, A. Weiß and M. Pfeiffer, *Organic, Hybrid, and Perovskite Photovoltaics XVIII*, SPIE, 2017, vol. 10363, pp. 29–33.
6 Certificate No. PV 60176081 - Certipedia, **https://www.certipedia.com/certificates/60176081?locale=en**, (accessed 10 October 2024).
7 O. L. Griffith, X. Liu, J. A. Amonoo, P. I. Djurovich, M. E. Thompson, P. F. Green and S. R. Forrest, Charge transport and exciton dissociation in organic solar cells consisting of dipolar donors mixed with ${\mathrm{C}}_{70}$, *Phys. Rev. B: Condens. Matter Mater. Phys.*, 2015, **92**, 085404.
8 X. Che, C.-L. Chung, C.-C. Hsu, F. Liu, K.-T. Wong and S. R. Forrest, Donor–Acceptor–Acceptor's Molecules for Vacuum-Deposited Organic Photovoltaics with Efficiency Exceeding 9%, *Adv. Energy Mater.*, 2018, **8**, 1703603.
9 V. Vohra, K. Kawashima, T. Kakara, T. Koganezawa, I. Osaka, K. Takimiya and H. Murata, Efficient inverted polymer solar cells employing favourable molecular orientation, *Nat. Photonics*, 2015, **9**, 403–408.
10 J. Zhao, Y. Li, G. Yang, K. Jiang, H. Lin, H. Ade, W. Ma and H. Yan, Efficient organic solar cells processed from hydrocarbon solvents, *Nat. Energy*, 2016, **1**, 1–7.
11 Y. Cui, Y. Xu, H. Yao, P. Bi, L. Hong, J. Zhang, Y. Zu, T. Zhang, J. Qin, J. Ren, Z. Chen, C. He, X. Hao, Z. Wei and J. Hou, Single-Junction Organic Photovoltaic Cell with 19% Efficiency, *Adv. Mater.*, 2021, **33**, 2102420.
12 Y. Wei, Z. Chen, G. Lu, N. Yu, C. Li, J. Gao, X. Gu, X. Hao, G. Lu, Z. Tang, J. Zhang, Z. Wei, X. Zhang and H. Huang, Binary Organic Solar Cells Breaking 19% via Manipulating the Vertical Component Distribution, *Adv. Mater.*, 2022, **34**, 2204718.
13 R. Sun, Y. Wu, X. Yang, Y. Gao, Z. Chen, K. Li, J. Qiao, T. Wang, J. Guo, C. Liu, X. Hao, H. Zhu and J. Min, Single-Junction Organic Solar Cells with 19.17% Efficiency Enabled by Introducing One Asymmetric Guest Acceptor, *Adv. Mater.*, 2022, **34**, 2110147.
14 L. Zhan, S. Li, Y. Li, R. Sun, J. Min, Y. Chen, J. Fang, C.-Q. Ma, G. Zhou, H. Zhu, L. Zuo, H. Qiu, S. Yin and H. Chen, Manipulating Charge Transfer and Transport via Intermediary Electron Acceptor Channels Enables 19.3% Efficiency Organic Photovoltaics, *Adv. Energy Mater.*, 2022, **12**, 2201076.
15 L. Zhu, M. Zhang, J. Xu, C. Li, J. Yan, G. Zhou, W. Zhong, T. Hao, J. Song, X. Xue, Z. Zhou, R. Zeng, H. Zhu, C.-C. Chen, R. C. I. MacKenzie, Y. Zou, J. Nelson, Y. Zhang, Y. Sun and F. Liu, Single-junction organic solar cells with over 19% efficiency enabled by a refined double-fibril network morphology, *Nat. Mater.*, 2022, **21**, 656–663.
16 P. Kaienburg, H. Bristow, A. Jungbluth, I. Habib, I. McCulloch, D. Beljonne and M. Riede, Vacuum-Deposited Donors for Low-Voltage-Loss Nonfullerene Organic Solar Cells, *ACS Appl. Mater. Interfaces*, 2023, **15**, 31684–31691.
17 P. Kaienburg, A. Jungbluth, I. Habib, S. V. Kesava, M. Nyman and M. K. Riede, Assessing the Photovoltaic Quality of Vacuum-Thermal Evaporated Organic Semiconductor Blends, *Adv. Mater.*, 2022, **34**, 2107584.
18 Z. Peng, N. Stingelin, H. Ade and J. J. Michels, A materials physics perspective on structure–processing–function relations in blends of organic semiconductors, *Nat. Rev. Mater.*, 2023, **8**, 439–455.
19 X. Yang, J. Loos, S. C. Veenstra, W. J. H. Verhees, M. M. Wienk, J. M. Kroon, M. A. J. Michels and R. A. J. Janssen, Nanoscale Morphology of High-Performance Polymer Solar Cells, *Nano Lett.*, 2005, **5**, 579–583.
20 K. Sun, Z. Xiao, S. Lu, W. Zajaczkowski, W. Pisula, E. Hanssen, J. M. White, R. M. Williamson, J. Subbiah, J. Ouyang, A. B. Holmes, W. W. H. Wong and D. J. Jones, A molecular nematic liquid crystalline material for high-performance organic photovoltaics, *Nat. Commun.*, 2015, **6**, 6013.
21 L. Ye, S. Li, X. Liu, S. Zhang, M. Ghasemi, Y. Xiong, J. Hou and H. Ade, Quenching to the Percolation Threshold in Organic Solar Cells, *Joule*, 2019, **3**, 443–458.
22 M. Ghasemi, H. Hu, Z. Peng, J. J. Rech, I. Angunawela, J. H. Carpenter, S. J. Stuard, A. Wadsworth, I. McCulloch, W. You and H. Ade, Delineation of Thermodynamic and Kinetic Factors that Control Stability in Non-fullerene Organic Solar Cells, *Joule*, 2019, **3**, 1328–1348.
23 L. Zhu, M. Zhang, G. Zhou, T. Hao, J. Xu, J. Wang, C. Qiu, N. Prine, J. Ali, W. Feng, X. Gu, Z. Ma, Z. Tang, H. Zhu, L. Ying, Y. Zhang and F. Liu, Efficient Organic Solar Cell with 16.88% Efficiency Enabled by Refined Acceptor Crystallization and Morphology with Improved Charge Transfer and Transport Properties, *Adv. Energy Mater.*, 2020, **10**, 1904234.
24 X. Dong, Y. Jiang, L. Sun, F. Qin, X. Zhou, X. Lu, W. Wang and Y. Zhou, Large-Area Organic Solar Modules with Efficiency Over 14%, *Adv. Funct. Mater.*, 2022, **32**, 2110209.

25 Y. Qin, Y. Xu, Z. Peng, J. Hou and H. Ade, Low Temperature Aggregation Transitions in N3 and Y6 Acceptors Enable Double-Annealing Method That Yields Hierarchical Morphology and Superior Efficiency in Nonfullerene Organic Solar Cells, *Adv. Funct. Mater.*, 2020, **30**, 2005011.
26 W. Zhu, A. P. Spencer, S. Mukherjee, J. M. Alzola, V. K. Sangwan, S. H. Amsterdam, S. M. Swick, L. O. Jones, M. C. Heiber, A. A. Herzing, G. Li, C. L. Stern, D. M. DeLongchamp, K. L. Kohlstedt, M. C. Hersam, G. C. Schatz, M. R. Wasielewski, L. X. Chen, A. Facchetti and T. J. Marks, Crystallography, Morphology, Electronic Structure, and Transport in Non-Fullerene/Non-Indacenodithienothiophene Polymer:Y6 Solar Cells, *J. Am. Chem. Soc.*, 2020, **142**, 14532–14547.
27 Y. Zhou, T. Taima, T. Miyadera, T. Yamanari, M. Kitamura, K. Nakatsu and Y. Yoshida, Phase separation of co-evaporated ZnPc:C60 blend film for highly efficient organic photovoltaics, *Appl. Phys. Lett.*, 2012, **100**, 233302.
28 L. Wang, S. Guo, K. Zhou and W. Ma, Control of the molecular orientation in small molecule-based organic photovoltaics, *Sustainable Energy Fuels*, 2020, **4**, 4934–4955.
29 E. Bittrich, J. Domke, M. Levichkova, D. Jehnichen, L. Bittrich, A. Janke, P. Formanek, R. Hübner, P. Uhlmann, K.-J. Eichhorn, R. Forker, M. Gruenewald, M. Al-Hussein, T. Fritz and K. Walzer, Structural Templating of an Organic Solar Cell Absorber by Ellagic Acid To Tune Its Aggregation, Molecular Orientation, and Optical Properties, *ACS Appl. Energy Mater.*, 2021, **4**, 14273–14286.
30 T. Kaji, M. Zhang, S. Nakao, K. Iketaki, K. Yokoyama, C. W. Tang and M. Hiramoto, Co-evaporant Induced Crystalline Donor: Acceptor Blends in Organic Solar Cells, *Adv. Mater.*, 2011, **23**, 3320–3325.
31 T. Kaji, S. Nakao and M. Hiramoto, Effect of Co-evaporant Induced Crystallization on Needle Growth of Phthalocyanine Thin Films, *Mol. Cryst. Liq. Cryst.*, 2013, **578**, 63–67.
32 F. Holzmueller, L. Wilde, F. Wölzl, C. Koerner, K. Vandewal and K. Leo, Co-evaporant induced crystallization of zinc phthalocyanine:C60 blends for solar cells, *Org. Electron.*, 2015, **27**, 133–136.
33 M. Katayama, T. Kaji, S. Nakao and M. Hiramoto, Ultra-Thick Organic Pigment Layer Up to 10 μm Activated by Crystallization in Organic Photovoltaic Cells, *Front. Energy Res.*, 2020, **8**, DOI: **10.3389/fenrg.2020.00004**.
34 A. Ojala, A. Petersen, A. Fuchs, R. Lovrincic, C. Pölking, J. Trollmann, J. Hwang, C. Lennartz, H. Reichelt, H. W. Höffken, A. Pucci, P. Erk, T. Kirchartz and F. Würthner, Merocyanine/C60 Planar Heterojunction Solar Cells: Effect of Dye Orientation on Exciton Dissociation and Solar Cell Performance, *Adv. Funct. Mater.*, 2012, **22**, 86–96.
35 S. Limbu, K.-B. Park, J. Wu, H. Cha, S. Yun, S.-J. Lim, H. Yan, J. Luke, G. Ryu, C.-J. Heo, S. Kim, Y. W. Jin, J. R. Durrant and J.-S. Kim, Identifying the Molecular Origins of High-Performance in Organic Photodetectors Based on Highly Intermixed Bulk Heterojunction Blends, *ACS Nano*, 2021, **12**(1), 1217–1228, DOI: **10.1021/acsnano.0c08287**.
36 S. Pfuetzner, J. Meiss, A. Petrich, M. Riede and K. Leo, Thick C60:ZnPc bulk heterojunction solar cells with improved performance by film deposition on heated substrates, *Appl. Phys. Lett.*, 2009, **94**, 253303.
37 K.-C. Chiu, L.-T. Juey, C.-F. Su, S.-J. Tang, M.-N. Jong, S.-S. Wang, J.-S. Wang, C.-S. Yang and W.-C. Chou, Effects of source and substrate temperatures on the properties of ITO/CuPc/C60 heterostructure prepared by physical vapor deposition, *J. Cryst. Growth*, 2008, **310**, 1734–1738.
38 S. Ouro Djobo, L. Cattin, M. Morsli, A. Godoy, F. R. Diaz, M. A. del Valle and J. C. Bernède, Effect of the Substrate Temperature on the Performance of Small Molecule Organic Solar Cells, *AIP Conf. Proc.*, 2011, **1391**, 251–253, DOI: **10.1063/1.3646846**.
39 M. Levichkova, D. Wynands, A. A. Levin, K. Walzer, D. Hildebrandt, M. Pfeiffer, V. Janonis, M. Pranaitis, V. Kažukauskas, K. Leo and M. Riede, Dicyanovinyl sexithiophene as donor material in organic planar heterojunction solar cells: Morphological, optical, and electrical properties, *Org. Electron.*, 2011, **12**, 2243–2252.
40 Y. Zhou, T. Taima, Y. Shibata, T. Miyadera, T. Yamanari and Y. Yoshida, Controlled growth of dibenzotetraphenylperiflanthene thin films by varying substrate temperature for photovoltaic applications, *Sol. Energy Mater. Sol. Cells*, 2011, **95**, 2861–2866.
41 C.-T. Chou, W.-L. Tang, Y. Tai, C.-H. Lin, C.-H. J. Liu, L.-C. Chen and K.-H. Chen, Effect of substrate temperature on orientation of subphthalocyanine molecule in organic photovoltaic cells, *Thin Solid Films*, 2012, **520**, 2289–2292.
42 U. Hörmann, C. Lorch, A. Hinderhofer, A. Gerlach, M. Gruber, J. Kraus, B. Sykora, S. Grob, T. Linderl, A. Wilke, A. Opitz, R. Hansson, A. S. Anselmo, Y. Ozawa, Y. Nakayama, H. Ishii, N. Koch, E. Moons, F. Schreiber and W. Brütting, Voc from a Morphology Point of View: the Influence of Molecular Orientation on the Open Circuit Voltage of Organic Planar Heterojunction Solar Cells, *J. Phys. Chem. C*, 2014, **118**, 26462–26470.
43 C. Lorch, H. Frank, R. Banerjee, A. Hinderhofer, A. Gerlach, G. Li Destri and F. Schreiber, Controlling length-scales of the phase separation to optimize organic semiconductor blends, *Appl. Phys. Lett.*, 2015, **107**, 201903.
44 Y.-Q. Zheng, J. Zhang, F. Yang, T. Komino, B. Wei, J. Zhang, Z. Wang, W. Pu, C. Yang and C. Adachi, Influence of deposition substrate temperature on the morphology and molecular orientation of chloroaluminum phthalocyanine films as well the performance of organic photovoltaic cells, *Nanotechnology*, 2015, **26**, 405202.
45 H.-J. Song, J. Roh and C. Lee, Simultaneous Engineering of the Substrate Temperature and Mixing Ratio to Improve the Performance of Organic Photovoltaic Cells, *J. Nanosci. Nanotechnol.*, 2016, **16**, 5104–5108.
46 T. Kirchartz, T. Agostinelli, M. Campoy-Quiles, W. Gong and J. Nelson, Understanding the Thickness-Dependent Performance of Organic Bulk Heterojunction Solar Cells: The Influence of Mobility, Lifetime, and Space Charge, *J. Phys. Chem. Lett.*, 2012, **3**, 3470–3475.

47 Y. Firdaus, V. M. Le Corre, J. I. Khan, Z. Kan, F. Laquai, P. M. Beaujuge and T. D. Anthopoulos, Key Parameters Requirements for Non-Fullerene-Based Organic Solar Cells with Power Conversion Efficiency >20%, *Adv. Sci.*, 2019, **6**, 1802028.
48 A. Pivrikas, G. Juška, A. J. Mozer, M. Scharber, K. Arlauskas, N. S. Sariciftci, H. Stubb and R. Österbacka, Bimolecular Recombination Coefficient as a Sensitive Testing Parameter for Low-Mobility Solar-Cell Materials, *Phys. Rev. Lett.*, 2005, **94**, 176806.
49 C. Deibel, Charge carrier dissociation and recombination in polymer solar cells, *Phys. Status Solidi A*, 2009, **206**, 2731–2736.
50 Y. Jin, Z. Chen, S. Dong, N. Zheng, L. Ying, X.-F. Jiang, F. Liu, F. Huang and Y. Cao, A Novel Naphtho[1,2-*c*:5,6-*c*′]-Bis([1,2,5]Thiadiazole)-Based Narrow-Bandgap π-Conjugated Polymer with Power Conversion Efficiency Over 10%, *Adv. Mater.*, 2016, **28**, 9811–9818.
51 K. N. Schwarz, P. B. Geraghty, V. D. Mitchell, S.-U.-Z. Khan, O. J. Sandberg, N. Zarrabi, B. Kudisch, J. Subbiah, T. A. Smith, B. P. Rand, A. Armin, G. D. Scholes, D. J. Jones and K. P. Ghiggino, Reduced Recombination and Capacitor-like Charge Buildup in an Organic Heterojunction, *J. Am. Chem. Soc.*, 2020, **142**, 2562–2571.
52 S. M. Hosseini, N. Tokmoldin, Y. W. Lee, Y. Zou, H. Y. Woo, D. Neher and S. Shoaee, Putting Order into PM6:Y6 Solar Cells to Reduce the Langevin Recombination in 400 nm Thick Junction, *Sol. RRL*, 2020, **4**, 2000498.
53 M. Saladina, C. Wöpke, C. Göhler, I. Ramirez, O. Gerdes, C. Liu, N. Li, T. Heumüller, C. J. Brabec, K. Walzer, M. Pfeiffer and C. Deibel, 2022.
54 N. Sergeeva, S. Ullbrich, A. Hofacker, C. Koerner and K. Leo, Structural Defects in Donor-Acceptor Blends: Influence on the Performance of Organic Solar Cells, *Phys. Rev. Appl.*, 2018, **9**, 024039.
55 J. Wu, J. Lee, Y.-C. Chin, H. Yao, H. Cha, J. Luke, J. Hou, J.-S. Kim and J. R. Durrant, Exceptionally low charge trapping enables highly efficient organic bulk heterojunction solar cells, *Energy Environ. Sci.*, 2020, **13**, 2422–2430.
56 J. Wu, J. Luke, H. K. H. Lee, P. Shakya Tuladhar, H. Cha, S.-Y. Jang, W. C. Tsoi, M. Heeney, H. Kang, K. Lee, T. Kirchartz, J.-S. Kim and J. R. Durrant, Tail state limited photocurrent collection of thick photoactive layers in organic solar cells, *Nat. Commun.*, 2019, **10**, 5159.
57 J. Yuan, Y. Zhang, L. Zhou, G. Zhang, H.-L. Yip, T.-K. Lau, X. Lu, C. Zhu, H. Peng, P. A. Johnson, M. Leclerc, Y. Cao, J. Ulanski, Y. Li and Y. Zou, Single-Junction Organic Solar Cell with over 15% Efficiency Using Fused-Ring Acceptor with Electron-Deficient Core, *Joule*, 2019, **3**(4), 1140–1151, DOI: **10.1016/j.joule.2019.01.004**.
58 J. C. Blakesley and D. Neher, Relationship between energetic disorder and open-circuit voltage in bulk heterojunction organic solar cells, *Phys. Rev. B: Condens. Matter Mater. Phys.*, 2011, **84**, 075210.
59 R. C. I. MacKenzie, T. Kirchartz, G. F. A. Dibb and J. Nelson, Modeling Nongeminate Recombination in P3HT:PCBM Solar Cells, *J. Phys. Chem. C*, 2011, **115**, 9806–9813.
60 D. Rauh, C. Deibel and V. Dyakonov, Charge Density Dependent Nongeminate Recombination in Organic Bulk Heterojunction Solar Cells, *Adv. Funct. Mater.*, 2012, **22**, 3371–3377.
61 A. Hofacker and D. Neher, Dispersive and steady-state recombination in organic disordered semiconductors, *Phys. Rev. B*, 2017, **96**, 245204.
62 R. C. I. MacKenzie, C. G. Shuttle, M. L. Chabinyc and J. Nelson, Extracting Microscopic Device Parameters from Transient Photocurrent Measurements of P3HT:PCBM Solar Cells, *Adv. Energy Mater.*, 2012, **2**, 662–669.
63 M. Hußner, R. A. Pacalaj, G. Olaf Müller-Dieckert, C. Liu, Z. Zhou, N. Majeed, S. Greedy, I. Ramirez, N. Li, S. M. Hosseini, C. Uhrich, C. J. Brabec, J. R. Durrant, C. Deibel and R. C. I. MacKenzie, Machine Learning for Ultra High Throughput Screening of Organic Solar Cells: Solving the Needle in the Haystack Problem, *Adv. Energy Mater.*, 2024, **14**, 2303000.
64 R. Fitzner, E. Mena-Osteritz, A. Mishra, G. Schulz, E. Reinold, M. Weil, C. Körner, H. Ziehlke, C. Elschner, K. Leo, M. Riede, M. Pfeiffer, C. Uhrich and P. Bäuerle, Correlation of π-Conjugated Oligomer Structure with Film Morphology and Organic Solar Cell Performance, *J. Am. Chem. Soc.*, 2012, **134**, 11064–11067.
65 B. Maennig, J. Drechsel, D. Gebeyehu, P. Simon, F. Kozlowski, A. Werner, F. Li, S. Grundmann, S. Sonntag, M. Koch, K. Leo, M. Pfeiffer, H. Hoppe, D. Meissner, N. S. Sariciftci, I. Riedel, V. Dyakonov and J. Parisi, Organic p–i–n solar cells, *Appl. Phys. A: Mater. Sci. Process.*, 2004, **79**, 1–14.
66 X. Jiang, S. Grott, V. Körstgens, K. S. Wienhold, Z. Li, J. Zhang, C. R. Everett, M. Schwartzkopf, S. V. Roth and P. Müller-Buschbaum, Film Formation Kinetics of Polymer Donor and Nonfullerene Acceptor Active Layers During Printing Out of 1,2,4-Trimethylbenzene in Ambient Conditions, *Sol. RRL*, 2023, **7**, 2201077.
67 C. Schünemann, D. Wynands, K.-J. Eichhorn, M. Stamm, K. Leo and M. Riede, Evaluation and Control of the Orientation of Small Molecules for Strongly Absorbing Organic Thin Films, *J. Phys. Chem. C*, 2013, **117**, 11600–11609.
68 C. Elschner, M. Schrader, R. Fitzner, A. A. Levin, P. Bäuerle, D. Andrienko, K. Leo and M. Riede, Molecular ordering and charge transport in a dicyanovinyl-substituted quaterthiophene thin film, *RSC Adv.*, 2013, **3**, 12117–12123.
69 J. E. Heger, W. Chen, S. Yin, N. Li, V. Körstgens, C. J. Brett, W. Ohm, S. V. Roth and P. Müller-Buschbaum, Low-Temperature and Water-Based Biotemplating of Nanostructured Foam-Like Titania Films Using ß-Lactoglobulin, *Adv. Funct. Mater.*, 2022, **32**, 2113080.
70 Z. Peng, L. Ye and H. Ade, Understanding, quantifying, and controlling the molecular ordering of semiconducting polymers: from novices to experts and amorphous to perfect crystals, *Mater. Horiz.*, 2022, **9**, 577–606.

71 M. A. Reus, L. K. Reb, A. F. Weinzierl, C. L. Weindl, R. Guo, T. Xiao, M. Schwartzkopf, A. Chumakov, S. V. Roth and P. Müller-Buschbaum, Time-Resolved Orientation and Phase Analysis of Lead Halide Perovskite Film Annealing Probed by In Situ GIWAXS, *Adv. Opt. Mater.*, 2022, **10**, 2102722.

72 E. Gann, A. T. Young, B. A. Collins, H. Yan, J. Nasiatka, H. A. Padmore, H. Ade, A. Hexemer and C. Wang, Soft X-ray scattering facility at the Advanced Light Source with real-time data processing and analysis, *Rev. Sci. Instrum.*, 2012, **83**, 045110.

73 B. A. Collins, Z. Li, J. R. Tumbleston, E. Gann, C. R. McNeill and H. Ade, Absolute Measurement of Domain Composition and Nanoscale Size Distribution Explains Performance in PTB7:PC71BM Solar Cells, *Adv. Energy Mater.*, 2013, **3**, 65–74.

74 B. A. Collins and E. Gann, Resonant soft X-ray scattering in polymer science, *J. Polym. Sci.*, 2022, **60**, 1199–1243.

75 Y. Liu, J. Zhao, Z. Li, C. Mu, W. Ma, H. Hu, K. Jiang, H. Lin, H. Ade and H. Yan, Aggregation and morphology control enables multiple cases of high-efficiency polymer solar cells, *Nat. Commun.*, 2014, **5**, 5293.

76 Z. Hamid, A. Wadsworth, E. Rezasoltani, S. Holliday, M. Azzouzi, M. Neophytou, A. A. Y. Guilbert, Y. Dong, M. S. Little, S. Mukherjee, A. A. Herzing, H. Bristow, R. J. Kline, D. M. DeLongchamp, A. A. Bakulin, J. R. Durrant, J. Nelson and I. McCulloch, Influence of Polymer Aggregation and Liquid Immiscibility on Morphology Tuning by Varying Composition in PffBT4T-2DT/Nonfullerene Organic Solar Cells, *Adv. Energy Mater.*, 2020, **10**, 1903248.

77 R. Meerheim, C. Körner and K. Leo, Highly efficient organic multi-junction solar cells with a thiophene based donor material, *Appl. Phys. Lett.*, 2014, **105**, 063306.

78 W. Zhao, S. Li, H. Yao, S. Zhang, Y. Zhang, B. Yang and J. Hou, Molecular Optimization Enables over 13% Efficiency in Organic Solar Cells, *J. Am. Chem. Soc.*, 2017, **139**, 7148–7151.

79 D. Wynands, M. Levichkova, M. Riede, M. Pfeiffer, P. Baeuerle, R. Rentenberger, P. Denner and K. Leo, Correlation between morphology and performance of low bandgap oligothiophene:C60 mixed heterojunctions in organic solar cells, *J. Appl. Phys.*, 2010, **107**, 014517.

80 A. Classen, C. L. Chochos, L. Lüer, V. G. Gregoriou, J. Wortmann, A. Osvet, K. Forberich, I. McCulloch, T. Heumüller and C. J. Brabec, The role of exciton lifetime for charge generation in organic solar cells at negligible energy-level offsets, *Nat. Energy*, 2020, **5**, 711–719.

81 H. Cha, Y. Zheng, Y. Dong, H. H. Lee, J. Wu, H. Bristow, J. Zhang, H. K. H. Lee, W. C. Tsoi, A. A. Bakulin, I. McCulloch and J. R. Durrant, Exciton and Charge Carrier Dynamics in Highly Crystalline PTQ10:IDIC Organic Solar Cells, *Adv. Energy Mater.*, 2020, **10**, 2001149.

82 B. Xiao, P. Calado, R. C. I. MacKenzie, T. Kirchartz, J. Yan and J. Nelson, Relationship between Fill Factor and Light Intensity in Solar Cells Based on Organic Disordered Semiconductors: The Role of Tail States, *Phys. Rev. Appl.*, 2020, **14**, 024034.

83 C. G. Shuttle, A. Maurano, R. Hamilton, B. O'Regan, J. C. de Mello and J. R. Durrant, Charge extraction analysis of charge carrier densities in a polythiophene/fullerene solar cell: Analysis of the origin of the device dark current, *Appl. Phys. Lett.*, 2008, **93**, 183501.

84 C. G. Shuttle, B. O'Regan, A. M. Ballantyne, J. Nelson, D. D. C. Bradley, J. de Mello and J. R. Durrant, Experimental determination of the rate law for charge carrier decay in a polythiophene: Fullerene solar cell, *Appl. Phys. Lett.*, 2008, **92**, 093311.

85 A. Foertig, A. Wagenpfahl, T. Gerbich, D. Cheyns, V. Dyakonov and C. Deibel, Nongeminate Recombination in Planar and Bulk Heterojunction Organic Solar Cells, *Adv. Energy Mater.*, 2012, **2**, 1483–1489.

86 T. Kirchartz and J. Nelson, Meaning of reaction orders in polymer:fullerene solar cells, *Phys. Rev. B: Condens. Matter Mater. Phys.*, 2012, **86**(16), 165201, DOI: **10.1103/PhysRevB.86.165201**.

87 L. Perdigón-Toro, L. Q. Phuong, F. Eller, G. Freychet, E. Saglamkaya, J. I. Khan, Q. Wei, S. Zeiske, D. Kroh, S. Wedler, A. Köhler, A. Armin, F. Laquai, E. M. Herzig, Y. Zou, S. Shoaee and D. Neher, Understanding the Role of Order in Y-Series Non-Fullerene Solar Cells to Realize High Open-Circuit Voltages, *Adv. Energy Mater.*, 2022, **12**, 2103422.

88 S.-U.-Z. Khan, J. Bertrandie, M. Gui, A. Sharma, W. Alsufyani, J. F. Gorenflot, F. Laquai, D. Baran and B. P. Rand, Quantifying the effect of energetic disorder on organic solar cell energy loss, *Joule*, 2022, **6**(12), 2821–2834, DOI: **10.1016/j.joule.2022.10.012**.

89 S. M. Hosseini, S. Wilken, B. Sun, F. Huang, S. Y. Jeong, H. Y. Woo, V. Coropceanu and S. Shoaee, Relationship between Energetic Disorder and Reduced Recombination of Free Carriers in Organic Solar Cells, *Adv. Energy Mater.*, 2023, **13**(8), 2203576, DOI: **10.1002/aenm.202203576**.

90 J. Vollbrecht, V. V. Brus, S.-J. Ko, J. Lee, A. Karki, D. X. Cao, K. Cho, G. C. Bazan and T.-Q. Nguyen, Quantifying the Nongeminate Recombination Dynamics in Nonfullerene Bulk Heterojunction Organic Solar Cells, *Adv. Energy Mater.*, 2019, **9**, 1901438.

91 C. G. Shuttle, R. Hamilton, J. Nelson, B. C. O'Regan and J. R. Durrant, Measurement of Charge-Density Dependence of Carrier Mobility in an Organic Semiconductor Blend, *Adv. Funct. Mater.*, 2010, **20**, 698–702.

92 P. Kaienburg, U. Rau and T. Kirchartz, Extracting Information about the Electronic Quality of Organic Solar-Cell Absorbers from Fill Factor and Thickness, *Phys. Rev. Appl.*, 2016, **6**, 024001.

93 J. A. Röhr, T. Kirchartz and J. Nelson, On the correct interpretation of the low voltage regime in intrinsic single-carrier devices, *J. Phys.: Condens. Matter*, 2017, **29**, 205901.

94 J. A. Röhr, D. Moia, S. A. Haque, T. Kirchartz and J. Nelson, Exploring the validity and limitations of the Mott–Gurney law for charge-carrier mobility determination of semiconducting thin-films, *J. Phys.: Condens. Matter*, 2018, **30**, 105901.

95 R. A. Street, Localized state distribution and its effect on recombination in organic solar cells, *Phys. Rev. B: Condens. Matter Mater. Phys.*, 2011, **84**, 075208.
96 R. C. I. MacKenzie, C. G. Shuttle, G. F. Dibb, N. Treat, E. von Hauff, M. J. Robb, C. J. Hawker, M. L. Chabinyc and J. Nelson, Interpreting the Density of States Extracted from Organic Solar Cells Using Transient Photocurrent Measurements, *J. Phys. Chem. C*, 2013, **117**, 12407–12414.
97 B. Bernardo, D. Cheyns, B. Verreet, R. D. Schaller, B. P. Rand and N. C. Giebink, Delocalization and dielectric screening of charge transfer states in organic photovoltaic cells, *Nat. Commun.*, 2014, **5**, 3245.
98 S. Tscheuschner, H. Bässler, K. Huber and A. Köhler, A Combined Theoretical and Experimental Study of Dissociation of Charge Transfer States at the Donor–Acceptor Interface of Organic Solar Cells, *J. Phys. Chem. B*, 2015, **119**, 10359–10371.
99 S. Shoaee, M. P. Eng, E. Espíldora, J. L. Delgado, B. Campo, N. Martín, D. Vanderzande and J. R. Durrant, Influence of nanoscale phase separation on geminate versus bimolecular recombination in P3HT:fullerene blend films, *Energy Environ. Sci.*, 2010, **3**, 971–976.
100 S. D. Dimitrov, M. Azzouzi, J. Wu, J. Yao, Y. Dong, P. S. Tuladhar, B. C. Schroeder, E. R. Bittner, I. McCulloch, J. Nelson and J. R. Durrant, Spectroscopic Investigation of the Effect of Microstructure and Energetic Offset on the Nature of Interfacial Charge Transfer States in Polymer: Fullerene Blends, *J. Am. Chem. Soc.*, 2019, **141**, 4634–4643.
101 J. Yao, T. Kirchartz, M. S. Vezie, M. A. Faist, W. Gong, Z. He, H. Wu, J. Troughton, T. Watson, D. Bryant and J. Nelson, Quantifying Losses in Open-Circuit Voltage in Solution-Processable Solar Cells, *Phys. Rev. Appl.*, 2015, **4**, 014020.
102 Z. Zhou, S. Xu, J. Song, Y. Jin, Q. Yue, Y. Qian, F. Liu, F. Zhang and X. Zhu, High-efficiency small-molecule ternary solar cells with a hierarchical morphology enabled by synergizing fullerene and non-fullerene acceptors, *Nat. Energy*, 2018, **3**, 952–959.
103 A. Jungbluth, E. Cho, A. Privitera, K. M. Yallum, P. Kaienburg, A. E. Lauritzen, T. Derrien, S. V. Kesava, I. Habib, S. M. Pratik, N. Banerji, J.-L. Brédas, V. Coropceanu and M. Riede, Limiting factors for charge generation in low-offset fullerene-based organic solar cells, *Nat. Commun.*, 2024, **15**, 5488.
104 D. Bartesaghi, I. del, C. Pérez, J. Kniepert, S. Roland, M. Turbiez, D. Neher and L. J. A. Koster, Competition between recombination and extraction of free charges determines the fill factor of organic solar cells, *Nat. Commun.*, 2015, **6**, 7083.
105 D. Kiermasch, A. Baumann, M. Fischer, V. Dyakonov and K. Tvingstedt, Revisiting lifetimes from transient electrical characterization of thin film solar cells; a capacitive concern evaluated for silicon, organic and perovskite devices, *Energy Environ. Sci.*, 2018, **11**, 629–640.
106 T. M. Clarke, F. C. Jamieson and J. R. Durrant, Transient Absorption Studies of Bimolecular Recombination Dynamics in Polythiophene/Fullerene Blend Films, *J. Phys. Chem. C*, 2009, **113**, 20934–20941.
107 A. Maurano, C. G. Shuttle, R. Hamilton, A. M. Ballantyne, J. Nelson, W. Zhang, M. Heeney and J. R. Durrant, Transient Optoelectronic Analysis of Charge Carrier Losses in a Selenophene/Fullerene Blend Solar Cell, *J. Phys. Chem. C*, 2011, **115**, 5947–5957.
108 A. Melianas, V. Pranculis, D. Spoltore, J. Benduhn, O. Inganäs, V. Gulbinas, K. Vandewal and M. Kemerink, Charge Transport in Pure and Mixed Phases in Organic Solar Cells, *Adv. Energy Mater.*, 2017, **7**, 1700888.
109 P. Friederich, V. Meded, A. Poschlad, T. Neumann, V. Rodin, V. Stehr, F. Symalla, D. Danilov, G. Lüdemann, R. F. Fink, I. Kondov, F. von Wrochem and W. Wenzel, Molecular Origin of the Charge Carrier Mobility in Small Molecule Organic Semiconductors, *Adv. Funct. Mater.*, 2016, **26**, 5757–5763.
110 T. Moench, P. Friederich, F. Holzmueller, B. Rutkowski, J. Benduhn, T. Strunk, C. Koerner, K. Vandewal, A. Czyrska-Filemonowicz, W. Wenzel and K. Leo, Influence of Meso and Nanoscale Structure on the Properties of Highly Efficient Small Molecule Solar Cells, *Adv. Energy Mater.*, 2016, **6**, 1501280.
111 M. Riede, C. Uhrich, J. Widmer, R. Timmreck, D. Wynands, G. Schwartz, W.-M. Gnehr, D. Hildebrandt, A. Weiss, J. Hwang, S. Sundarraj, P. Erk, M. Pfeiffer and K. Leo, Efficient Organic Tandem Solar Cells based on Small Molecules, *Adv. Funct. Mater.*, 2011, **21**, 3019–3028.
112 X. Che, X. Xiao, J. D. Zimmerman, D. Fan and S. R. Forrest, High-Efficiency, Vacuum-Deposited, Small-Molecule Organic Tandem and Triple-Junction Photovoltaic Cells, *Adv. Energy Mater.*, 2014, **4**, 1400568.
113 R. Meerheim, C. Körner, B. Oesen and K. Leo, 10.4% Efficient triple organic solar cells containing near infrared absorbers, *Appl. Phys. Lett.*, 2016, **108**, 103302.
114 J. Meiss, M. Furno, S. Pfuetzner, K. Leo and M. Riede, Selective absorption enhancement in organic solar cells using light incoupling layers, *J. Appl. Phys.*, 2010, **107**, 053117.
115 Y. Dong, H. Cha, H. L. Bristow, J. Lee, A. Kumar, P. S. Tuladhar, I. McCulloch, A. A. Bakulin and J. R. Durrant, Correlating Charge-Transfer State Lifetimes with Material Energetics in Polymer:Non-Fullerene Acceptor Organic Solar Cells, *J. Am. Chem. Soc.*, 2021, **143**, 7599–7603.
116 L. Ye, H. Hu, M. Ghasemi, T. Wang, B. A. Collins, J.-H. Kim, K. Jiang, J. H. Carpenter, H. Li, Z. Li, T. McAfee, J. Zhao, X. Chen, J. L. Y. Lai, T. Ma, J.-L. Bredas, H. Yan and H. Ade, Quantitative relations between interaction parameter, miscibility and function in organic solar cells, *Nat. Mater.*, 2018, **17**, 253–260.
117 Z. Peng, N. Stingelin, H. Ade and J. J. Michels, A materials physics perspective on structure–processing–function relations in blends of organic semiconductors, *Nat. Rev. Mater.*, 2023, **8**, 439–455.

